Tribology Letters (2024) 72:105
https://doi.org/10.1007/s11249-024-01904-x

ORIGINAL PAPER

The Effects of Humidity on the Velocity-Dependence and Frictional Ageing of Nanoscale Silica Contacts

J. Brandon McClimon[2] · Zhuohan Li[1] · Khagendra Baral[1] · David Goldsby[3] · Izabela Szlufarska[1] · Robert W. Carpick[2]

Received: 12 September 2023 / Accepted: 5 August 2024

Abstract
This work examines the effect of environmental humidity on rate-and-state friction behavior of nanoscale silica-silica nanoscale contacts in an atomic force microscope, particularly, its effect on frictional ageing and velocity-weakening vs. strengthening friction from 10 nm/s to 100 µm/s sliding velocities. At extremely low humidities ($\ll 1\%RH$), ageing is nearly absent for up to 100 s of nominally stationary contact, and friction is strongly velocity-strengthening. This is consistent with dry interfacial friction, where thermal excitations help overcome static friction at low sliding velocities. At higher humidity levels (10–40% RH), ageing becomes pronounced and is accompanied by much higher kinetic friction and velocity-weakening behavior. This is attributed to water-catalyzed interfacial Si–O-Si bond formation. At the highest humidities examined (> 40% RH), ageing subsides, kinetic friction drops to low levels, and friction is velocity-strengthening again. These responses are attributed to intercalated water separating the interfaces, which precludes interfacial bonding. The trends in velocity-dependent friction are reproduced and explained using a computational multi-bond model. Our model explicitly simulates bond formation and bond-breaking, and the passivation and reactivation of reaction sites across the interface during sliding, where the activation energies for interfacial chemical reactions are dependent on humidity. These results provide potential insights into nanoscale mechanisms that may contribute to the humidity dependence observed in prior macroscale rock friction studies. They also provide a possible microphysical foundation to understand the role of water in interfacial systems with water-catalyzed bonding reactions, and demonstrate a profound change in the interfacial physics near and above saturated humidity conditions.

Keywords RSF · Silica · Ageing · AFM · Humidity dependence

1 Introduction

Rate-and-state friction (RSF), like Coulomb and Amontonian friction, consists of a set of empirical laws describing the frictional response of materials [1]. While RSF behavior was discovered and described much later than the other friction laws, it has been found to apply to a broad range of materials [2], from rocks to paper to hydrogels. Within the RSF framework, friction can be described by an equation of the form

$$\mu = \mu_0 + a \ln \frac{V}{V_0} + b \ln \frac{V_0 \theta}{D_c} \quad (1)$$

where μ is the friction coefficient, μ_0 is the steady-state friction coefficient at a reference velocity V_0, V is the current sliding velocity, D_c is the so-called "memory distance" which is the characteristic sliding distance over which transients empirically evolve [3, 4], a and b are empirical constants, and θ is a state variable which has units of time. Note: for consistency with the RSF literature ("velocity-weakening" etc.), we use the term velocity throughout, but in all cases we are referring to the magnitude of the velocity, i.e., the speed. The second term on the righthand side of Eq. 1 is

J. Brandon McClimon and Zhuohan Li have contributed equally to the present work.

✉ Robert W. Carpick
carpick@seas.upenn.edu

[1] Department of Materials Science and Engineering, University of Wisconsin, Madison, WI, USA

[2] Department of Mechanical Engineering and Applied Mechanics, University of Pennsylvania, Philadelphia, PA, USA

[3] Department of Earth and Environmental Science, University of Pennsylvania, Philadelphia, PA, USA

Published online: 19 August 2024

referred to as the direct effect, since it describes how friction changes in direct response to a change in sliding velocity (for example, friction increases (decreases) abruptly with a step increase (decrease) in sliding velocity); the third term is the evolution effect, so-named because the state variable θ in this term evolves over time (or with slip) with a change in sliding velocity. This term also describes static ageing, a characteristic phenomenon in RSF where the magnitude of static friction grows with time due to a time-dependent growth in the magnitude of θ.

A basic prediction of this law is that during steady-state sliding, μ varies linearly with the logarithm of velocity with a slope of $a - b$. Additionally, the frictional response is invariably mediated via the elastic coupling between the application point of a lateral stress and the sliding interface (e.g., torsion of the atomic force microscope (AFM) cantilever in this study) which can give rise to complex overall behaviors such as stick–slip motion [5–7]; note that this type of stick–slip is not due to the position-dependent potential energy corrugation that leads to atomic lattice stick–slip motion [8], but rather, is due to an increase in static friction with time in stationary contact (static ageing) [6], and/or a decrease in kinetic friction with slip speed (evolution effect) [5].

A hallmark of RSF is the history dependence of friction, which is described analytically with a state variable. The evolution of state with time is typically described by either of two equations, the slowness law and the slip law. The slowness law, attributed to Dietrich, is given by Ref. [9]:

$$\frac{d\theta}{dt} = 1 - \frac{V\theta}{D_c} \tag{2}$$

and the slip law, attributed to Rice and Ruina, is given by Ref. [7]

$$\frac{d\theta}{dt} = -\frac{V\theta}{D_c} \ln\left(\frac{V\theta}{D_c}\right) \tag{3}$$

The slowness law differs fundamentally from the slip law in that it allows the state to increase with the time of stationary contact during a hold, whereas the slip law requires slip to increase the state [1].

The physical basis of these and other laws describing RSF behavior is still debated [10–13], particularly with regard to the physical meaning of state, with multiple mechanisms having different degrees of empirical and theoretical support. Given the complexity of real macroscale and geoscale contacts it is likely that multiple mechanisms contribute [14, 15]. The canonical view in the rock physics community is that the state variable represents the real area of contact at a frictional interface, which increases with the time of stationary contact due to plastic creep of asperities, with a number of macroscale studies demonstrating it's existence [16, 17]. This mechanism leads to rate-and-state response in other material systems such as polymers [10, 11, 18–20].

Another proposed mechanism for RSF is one that emerges from the rheology of granular packings [12]. Such an interfacial geometry is ubiquitous in the particulate gouge found at geological faults. The primary prediction is that the coefficient of friction is determined by a dimensionless "inertial number" that depends upon the shear rate and the confining pressure [12]. Despite the absence of time-dependent friction (i.e., RSF response) between contacting grains in the simulations, the authors were able to reproduce many features of the RSF response including time-dependent static strengthening attributed to stronger inter-particle coupling with slow compaction [12]. To date, however, such simulations have not been able to reproduce velocity-weakening friction, which is commonly observed in rock friction experiments and considered to be a necessary condition for earthquake nucleation [5, 7].

The evolution of state may also be due to increases in the frictional strength (i.e., in the shear strength) of the contacts, instead of increases in contact area as described above. In particular, silica-silica interfaces are known to form bonds, including covalent siloxane (Si–O–Si) bonds [21, 22]. At the nanoscale, this has been shown to result in a corresponding increase in static friction [21, 23–26]. This is referred to as interfacial chemical bond-induced (ICBI) friction at the nanoscale. In the case of nanoscale silica-silica contacts, ICBI has been shown to be due to the formation of strong siloxane bonds between hydrated silica surfaces. Our earlier work employed AFM to examine this phenomenon for nanoscale silica contacts wherein plastic deformation and creep of the contacts were negligible [21, 23–26]. The frictional strength of these contacts increases with the logarithm of the hold time, consistent with the slowness law, and complementary simulations demonstrate how this logarithmic rate of chemical bonding arises from a combination of a distribution of activation barriers to bonding and an antagonistic interaction effect between bonding at neighboring sites [23]. Since then, we and others have shown how the slowness law can be derived from the ICBI mechanism [24, 27], demonstrated how this mechanism can lead to stick–slip friction, another hallmark of RSF [25], and examined how this nanoscale phenomenon can manifest in more complex macroscale contacts [28, 29]. Finally, it was also shown that ICBI mechanism can in fact lead to increase not only of the shear strength, but also of the real contact area, both contributing to the logarithmic increase of static friction with time [30].

An important aspect of the RSF response is the role of water, especially in the case of interfacial chemical bonding. The presence of ambient water is known to control the density of thermodynamically favored hydroxyl terminated sites on the surface of silica, as well as other geologically

relevant minerals [31–33]. Hydroxyl groups participate directly in the interfacial bonding reactions responsible for ICBI [21, 23, 34]. Empirically, it is known that humidity has a strong effect on the frictional behavior of rocks, and is necessary for the evolution of state [35, 36]. Trends in the frictional response of materials with changing humidity are not universal, and depend on the specific material system, interface morphology, and testing protocol. For macroscale experiments, steady-state friction has been found to either decrease [35, 37–39] or remain static [36, 38] with increasing humidity. Additionally, increasing humidity often leads to enhancements in static ageing [21, 35, 36] and unstable sliding [35, 36], as characterized by velocity-weakening or the observation of stick–slip. Intriguingly, macroscale experiments on quartz rocks [35] at RH < 1% and quartz powders [36] at RH < 5% show an absence of state evolution in slide-hold-slide experiments. These results were attributed to a humidity dependence of the mechanical creep of quartz. However, some of the present authors recently showed using nanoindentation that a quartz sample does not show any humidity-dependent mechanical creep up to 50% RH [40]. This demonstrates that the humidity dependence of the frictional ageing of quartz cannot be explained by asperity creep, and instead indicates that other humidity-dependent mechanisms, including time-dependent chemical bond formation or slip-induced strengthening, are at play.

Theoretical examination of the relevant chemistry between SiO_2 interfaces has revealed that water can play an important role. First principles molecular dynamics (FPMD) calculations which were based on density functional theory (DFT) and therefore captured electronic interactions, were utilized to study the role of water during wear of sliding quartz slabs by Ootani et al. [34] This study showed that the activation energy for interfacial bonding is reduced by 72% when water molecules participate in the reaction, as shown in Fig. 1, adapted from Ootani et al. [34] In these simulations, nearby water molecules facilitated the reaction by functioning as proton receptors, forming H_3O^+ and leaving a reactive SiO^- ion termination at the silica surface, which subsequently could form an interfacial covalent bond. The scheme in the lower panel of Fig. 1 is one example of such a water-facilitated reaction, but the water-mediated proton transfer was a common feature in the formation of all interfacial bonds observed in the aforementioned simulations. The much lower activation energy for interfacial bond formation when water was present to act as a proton acceptor suggests that water allows for much more rapid interfacial bonding kinetics. The same H_2O proton acceptor mechanism for the formation of interfacial Si–O–Si bonds was found to be operative in another study using classical MD with the ReaxFF force field [41], and in the Si_3N_4 and SiC material systems [42]. Experimental studies of nanoscale wear in silica systems have found accelerated wear with increasing humidity, which is consistent with an increased rate of interfacial bonding due to elevated humidity [43, 44].

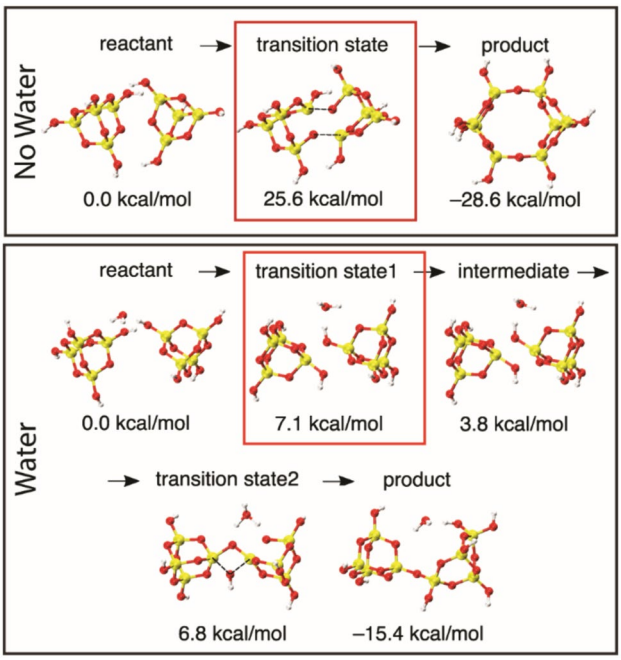

Fig. 1 Possible reaction paths leading to SiO_2 interfacial bonding with activation energies, dependent upon participation of water molecules. Adapted from Ref. [31]. Note: images here isolated from full simulation geometry of two quartz slabs, each composed of 165 atoms

We have previously demonstrated that the interfacial chemical bonding mechanism can provide a physical basis for friction behavior that follows the slowness law in nanoscale silica-silica contacts [15, 21, 23–26, 28, 29], just as mechanical creep did before it. Further investigations of this mechanism are warranted. In particular, the influence of humidity on interfacial bonding and the resulting RSF effects in nanoscale silica-silica contacts, the subjects of this study, have not been established. We are further motivated by the fact that a nanoscale system remains the best way experimentally to test whether RSF behavior can occur in the absence of significant plastic deformation and granular dynamics effects (as opposed to larger length scales where these effects, and others, typically are present), i.e., to show that chemical bonding alone can lead to RSF-like behavior.

2 Experimental Methods

All experiments were performed in an RHK350 AFM mounted in a vacuum chamber (RHK Technologies, Troy, MI), but with pressures ranging from 1 atm to 0.09 mbar. In experiments at atmospheric pressure, humidity was controlled by mixing clean, dry N_2 gas from the boiloff of

a liquid nitrogen Dewar with moist N_2 gas that had been directed through a deionized water-filled bubbler. Relative humidity was monitored via a hygrometer (FisherBrand traceable hygrometer/thermometer/dew point meter, Fisher Scientific, Pittsburgh, PA) with its probe located inside the vacuum chamber. In the experiments under vacuum, the chamber was exposed to ambient air conditions overnight then sealed and pumped with a scroll pump until the desired pressure was achieved. The pump was deenergized and the chamber isolated prior to the AFM measurements. For the slide-hold-slide experiments under reduced pressure, the pressure was progressively lowered while measuring the ageing response at particular pressures; a final test was performed again after venting to atmospheric pressure to confirm the ageing response did not change significantly during the testing due to tip wear or sample reactivity changes.

All experiments were performed with commercial Si AFM probes (PPP-FM, Nanosensors, Neuchatel, Switzerland) and polished Si wafer samples (El-Cat, Ridgefield Park, NJ) which were both subjected to annealing in a quartz tube furnace at 1000°C for 20 min in ambient air, 30–50% RH, to grow an oxide coating with a thickness > 20 nm, confirmed with post-annealing TEM imaging of the AFM probes. Dedicated quartz tubes were used for all annealing runs to ensure no contaminants from the furnace annealing of other samples was present. The probes and samples remained in the furnace during heatup and cooldown. This temperature led to little blunting of the probes with post-annealing tip radii of 15–25 nm based on blind tip reconstruction and TEM imaging (see SI), whereas we found empirically that similar annealing times at 1100°C led to final tip radii larger than 100 nm. Prior to each experiment, the silica sample was cleaned via O_2 plasma for 5 min, both to remove hydrocarbon contamination and maximize the density of hydroxyl group terminations on the silica surface [45]. We note that the wafers are phosphorous-doped at a level of 1×10^{15} cm^{-3} because they are produced for semiconductor applications; at this doping level a concentration of only 1 P dopant per 1×10^6 nm^2 is expected even before the surface is oxidized. Thus, the dopants play no role in the experimental behavior. The AFM probes were calibrated for normal forces using the Sader method [46], and for lateral forces using the diamagnetic lateral force calibration technique [47].

Slide-hold-slide experiments were performed by laterally translating the probes in a reciprocating path on the substrate across a 500-nm track at 50 nm/s and zero applied load (maintained using the AFM's normal force feedback control). Zero applied load was used to ensure contact pressures remained well below the hardness value of the silica counterfaces, as confirmed in a prior study with similarly prepared probes and substrates [21]. Kinetic friction values were stable at steady-state, without any evidence of a stick–slip response that would necessitate stability analysis [48]. Holds were performed by stopping the lateral translation at the center of the track for the specified hold time, then continuing in the same direction at 50 nm/s. Values for the friction drop, from peak static friction after the holds to lower friction when sliding begins, were measured from the lateral force vs. lateral translation data, as demonstrated in the inset of Fig. 2a. The friction drop is a common measure used to quantify the ageing magnitude [21, 23]. Hereafter, the ageing response will be referred to as "ageing response ΔF". Each reported average value and standard deviation were calculated from at least 8 slide-hold-slide cycles. The order in which holds of different times were performed was randomized to prevent the possibility of a systematically changing tip geometry and thereby affecting the results. The lack of

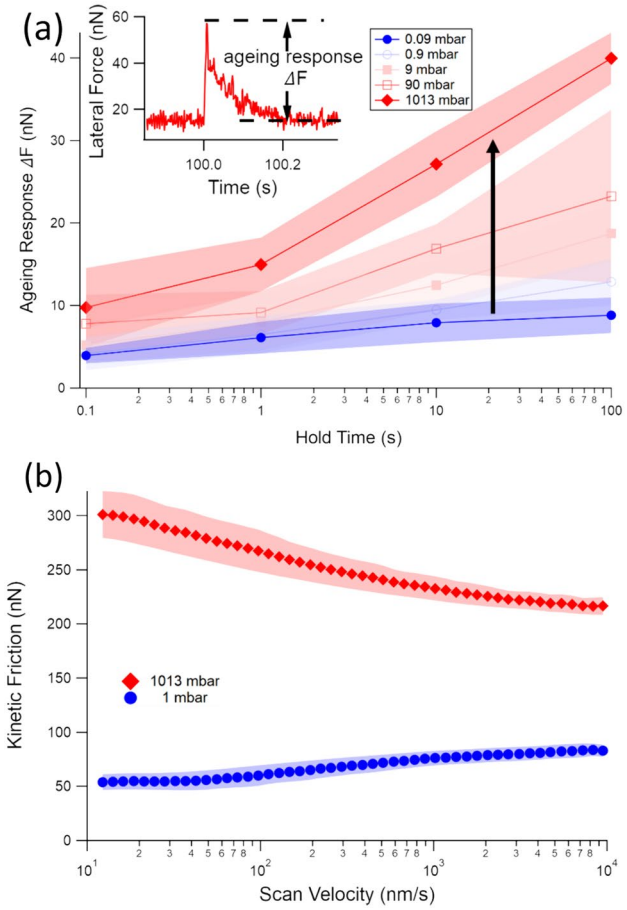

Fig. 2 **a** Ageing response ΔF as a function of hold time in a slide-hold-slide experiment as a function of ambient total pressure in air. Colored shading shows the standard deviation of the values captured from eight sequential sliding cycles. The inset demonstrates how the ageing response ΔF (friction drop) was measured at the end of the hold time. The arrow illustrates the trend with increasing pressure/humidity. **b** Velocity-dependence of kinetic friction for different total pressures in air

such a sequence-dependence in the slide-hold-slide ageing response also provides further reassurance that plastic creep of the asperity could be effectively excluded as a physical mechanism for ageing in these experiments. Adhesion was also periodically measured via the maximal adhesion force during force-distance curves where the probe approached the surface at a rate of 100 nm/s up to a maximum load of ~ 20 nN, then retracted at the same rate.

Using blind tip reconstruction [49] before and after experiments, the wear rates of the AFM probes in the SiO_2 system were found to be excessive at intermediate humidity levels. For context, a probe with an initial radius of 63 nm was slid for 32 µm at zero applied load at 10% RH during conventional speed-dependence testing and experienced 4 nm of vertical wear resulting in a punch shape with a 50 nm diameter. To give a sense of how little sliding this is, a single 100×100 nm^2 image with 256 lines experiences 51 µm of sliding; a well-functioning AFM tip should be able to acquire many such images without appreciable wear [43]. This led to difficulty in extracting repeatable trends for the velocity-dependence of friction across multiple humidity levels when measured in the typical way of performing contact mode imaging at each sliding velocity.

To deal with this difficulty, a new protocol was developed which involved continuously varying the sliding velocity across the entire velocity range in a single scan line. This technique and the associated analysis are detailed in the Supplemental Information. To ensure that the track length was long enough to maintain steady-state conditions at all velocities (i.e., negligible transient history effects on kinetic friction due to RSF behavior), the protocol was performed on 1 and 2-µm long tracks, and equivalent results were obtained for the two track lengths. All velocity-dependent friction results reported from this are the average values and standard deviations obtained from at least three sliding cycles. The only exception is where individual cycles are reported to demonstrate a repeatable evolution effect across the test. This protocol minimized the amount of sliding required to capture each velocity-dependence curve and therefore minimized cumulative tip wear, allowing for repeatable results across a succession of humidity levels. This also allowed for a high density of data in each curve (e.g., the 1013 mbar trace in Fig. 2b), which is composed of 50 data points, each of which is an average across a 40 nm track length and a small range of velocity). For the load-dependent kinetic friction tests discussed later, the load was progressively increased to the maximum load while measuring the speed-dependence of kinetic friction at select loads, and then lowered progressively back to zero applied load while repeating the kinetic friction tests at the same loads to confirm a similar response was achieved.

3 Experimental Results

Figure 2a shows the trends in ageing response ΔF from slide-hold-slide measurements under varying total pressure of ambient air for hold times of 0.1, 1, 10, and 100 s, with a partial pressure of water corresponding to $16 \pm 2\%$ RH at ambient pressure (1013 mbar). In this nanoscale silica system, the ageing response ΔF increases approximately linearly with the logarithm of the hold time for hold times between 1 and 100 s. The increasing slope of the curves in Fig. 2a with increasing total pressure can be attributed to an increase in the availability of water to participate in the interfacial bonding reaction (other constituents of the ambient environment such as nitrogen and argon are not expected to participate). The decline of static ageing on timescales above several seconds in highly inert, UHV environments has been reported in other AFM studies [50, 51].

Figure 2b shows velocity-dependence of the kinetic friction at the two extremes of pressure in Fig. 2a, across sliding velocities from 10 nm/s to 10 µm/s. The overall shapes of the curves are similar to what has been seen in macroscale rock friction experiments [1], with a near-linear dependence on the logarithm of the sliding velocity (V). At the lowest total pressure (1 mbar), we observed mildly velocity-strengthening behavior, whereas at the highest total pressure (1013 mbar) we observe a strong velocity-weakening trend. The observed change in the velocity-dependence can again be attributed to the availability of water molecules to participate in the interfacial bonding reaction. At low pressure, water is unavailable, so interfacial bonding is largely precluded. This in turn results in low overall friction and a velocity-dependence of friction that is dominated by the direct effect in the framework of RSF. Specifically, the increase of kinetic friction with log V in a non-bonding nanoscale system is well understood to be due to thermally activated jumps between adjacent energy minima in the potential energy landscape, with thermal activation becoming less effective with increasing load-point velocity [52, 53]. In contrast, at the highest total pressure, water is readily available to participate in interfacial bonding, which results in higher overall friction due to the presence of many interfacial bonds. The velocity-weakening behavior can be rationalized in simple fashion under the assumption of a constant bond formation rate for these short-lived contact sites [54]: each possible bonding site on the tip traverses more of the sample surface in an unbonded state at higher sliding velocities, thereby lowering the average friction with increasing sliding velocity. The approximately linear dependence on the logarithm of velocity is typical of RSF behavior [27].

To access higher humidity levels, similar experiments were performed at varying % RH at ambient pressure in

N_2. The ageing and velocity-dependent behavior show non-monotonicity at these higher humidity levels. Figure 3a shows the ageing response ΔF for 1–60 ± 2% RH. The arrows are added to emphasize the non-monotonicity. At the lowest humidity, the ageing response ΔF is weak, consistent with data shown in Fig. 2a. For humidities in the range 10–40 ± 2% RH, the ageing response ΔF is approximately constant, and at 60 ± 2% RH the ageing response ΔF is again subdued. The inset of Fig. 3a shows the trend in adhesion across the same humidity range. The adhesion varies substantially across this range. This variation can be attributed primarily to capillary formation between the tip and the sample and is consistent with previous literature [55–57]. The non-monotonic change in adhesion with %RH is typical in the literature [58, 59], and has often been attributed to the formation of a load-bearing ice-like water layer at the sample surface which causes a reduction of adhesion at high humidity. This phenomenon can also rationalize the friction and ageing seen in Fig. 3. Separation of the two silica surfaces by an ice-like layer would prevent the formation of interfacial chemical bonds. This prevents ageing (Fig. 3a) and chemical bonding during sliding (Fig. 3b), which leaves only a velocity-strengthening Prandtl-Tomlinson type friction response.

Figure 3b shows the velocity-dependence of kinetic friction. Similar to the trend shown in Fig. 3a, the trend in kinetic friction is also nonmonotonic with humidity (as indicated by the arrows). At 1 ± 2% RH, friction is relatively low and independent of velocity. When the humidity increased to 10 ± 2% RH, the overall friction became high and strongly velocity-weakening across the entire velocity range, which extends to 100 μm/s. As the % RH is raised further, the overall friction decreased and velocity-weakening became less and less pronounced until velocity-strengthening (and low friction) was observed again at 60 ± 2% RH. It should be noted at this point that while these qualitative trends were easily reproducible, the % RH corresponding to the maximum friction and to the regime of velocity-weakening could vary from 5 to 20% RH between experiments [21, 60, 61]. This variation can be attributed to the difficulty of maintaining a perfectly reproducible SiO_2 surface chemistry and thus sample reactivity. After plasma cleaning, the surface hydroxyl density decreases substantially on the timescale of hours due to adsorption of hydrocarbon molecules present in ambient air, which reduces the density of hydroxyl sites available for interfacial bonding [45, 62].

To better understand the transition from velocity-strengthening to velocity-weakening friction at low % RH, velocity-dependence testing was performed at a succession of closely spaced humidity levels. The results are shown in Fig. 4. At each humidity level there is a transition velocity where the

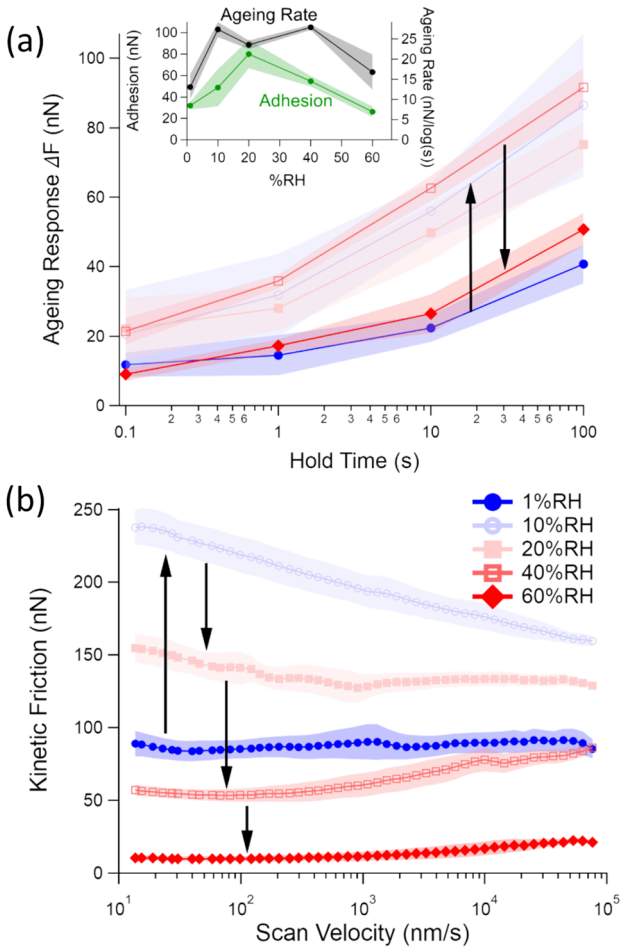

Fig. 3 **a** Ageing response during slide-hold-slide measurements performed in different ambient humidities. Inset shows adhesion trend across same humidity range. **b** Velocity-dependence of kinetic friction across same humidity range as (**a**)

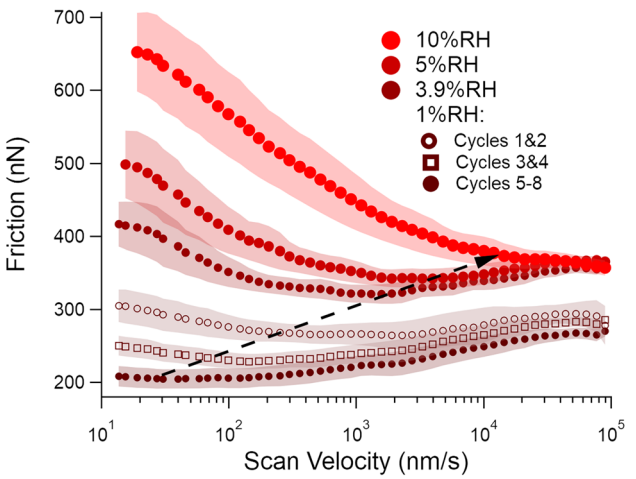

Fig. 4 Velocity-dependence of kinetic friction at a succession of humidity levels between 1 and 10% RH. The dashed arrow highlights the trend in the transition velocity between velocity-weakening and strengthening

trend switches from velocity-weakening to velocity-strengthening. This effect has been observed in other studies [63, 64] but is inconsistent with the most common forms of the RSF laws [5, 65, 66]. Such a transition velocity could have important effects in earthquake mechanics, such as promoting stable slip and limiting the magnitude of slip events [5, 63, 67, 68]. As the humidity level rises, this transition velocity shifts to higher and higher values, as highlighted by the black dashed arrow. The velocity-dependence testing protocol (see SI for more details) involved traversing the entire velocity range during each sliding cycle, with eight cycles performed sequentially in a reciprocating fashion on the same, initially unworn wear track. The test at 1 ± 2% RH, unlike the data shown for the other humidities where data from all cycles were averaged, is subdivided into averages of cycles 1 and 2, 3 and 4, and 5 through 8. The data were subdivided in this way because we typically observed an evolution of the friction at this % RH during the test, with friction decreasing at the lowest sliding velocities during the test. This effect was not observed at higher humidities. Another example of the cycle dependence at low % RH is shown in the SI. We hypothesize that as the test proceeds, adsorbed water molecules are progressively removed from the wear track, leading to a reduced inventory of water that can participate in interfacial chemical bonding.

We hypothesized that the shift to lower, velocity-strengthening kinetic friction and a weaker ageing response at high % RH (e.g., 60% RH in Fig. 3a, b) was due to a water layer that separates the counterfaces and precludes interfacial bonding; such a trend was recently found in AFM measurements on highly oriented pyrolytic graphite samples [69] and an ice-like layer is expected to form on hydrophilic silica [58]. If this hypothesis is valid, there must be some normal pressure that displaces this water and reimposes velocity-weakening friction. A simple test of this would be to measure the velocity-dependence at a succession of increasing normal loads, where the reappearance of velocity-weakening behavior would indicate that interfacial bonds are again forming between the counterfaces. An example of such a test, performed at 60 ± 2% RH, is shown in Fig. 5. At zero applied load, friction is velocity-strengthening, but as the applied load is increased, the behavior becomes velocity-weakening, consistent with a mechanism of interfacial water preventing covalent bond formation between the counterfaces. Our results are consistent with a previous experimental result obtained for a silica-silica interface immersed in an ionic liquid (IL) [70], where the authors observed that the velocity-weakening trend is obtained only at a relatively high contact pressure range (> 1.1 GPa). This phenomenon was attributed to the expulsion of the confined IL film from the contact, which exposes the surface silanol groups and facilitates the formation of interfacial siloxane bonds. Blind tip reconstruction [49] of the tip after this high-load testing

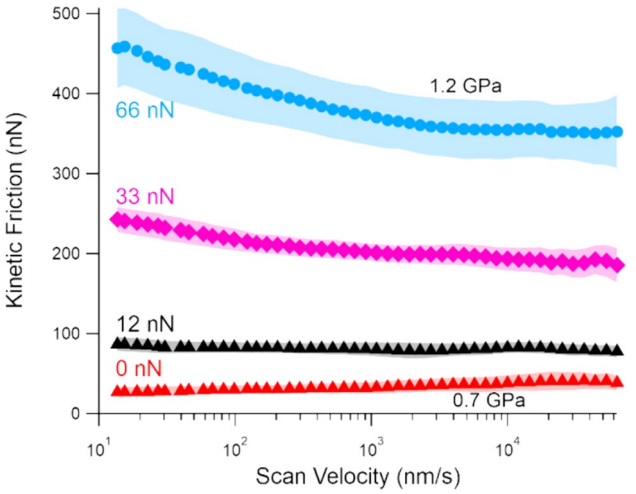

Fig. 5 Velocity-dependence of kinetic friction as a function of applied normal load in 60 ± 2% RH N_2 environment

revealed a blunted but still hemispherical geometry (see SI). From this final geometry, the DMT model [71] was used to estimate the nominal contact pressure at each load, the highest and lowest of which are annotated in Fig. 5. These contact pressures are likely underestimated, however, since while the tip apex geometry was approximately spherical, we show next that friction *vs.* load scaling is linear, which implies that the contact involves multiple asperities. The finding that it requires > 1 GPa of contact pressure to reimpose velocity-weakening friction shows that the water layer between the counterfaces possesses a substantial load-bearing capacity. Similar load-dependencies have been observed previously [72].

We also considered stress enhancement of the interfacial bonding rate as an explanation for the transition from velocity-strengthening to velocity-weakening friction in Fig. 5. If such an effect was significant, at low contact pressures where interfacial bonding is slow, velocity-weakening friction would be observed as a consequence of dominant Prandtl-Tomlinson friction, but at higher contact pressures interfacial bonding would be dominant, leading to a velocity-weakening response. This is what we see in Fig. 5. To examine this possibility, we can use the insights from the load-dependence of friction on load. If the rate of bonding was sensitive to the contact stress in the relevant load range, one would expect a supralinear scaling of friction vs. load. This is because more bonds would form within each unit of real contact area, thereby increasing friction. An earlier study examined the load-dependence of friction in the same material system and found a linear scaling of friction with load [24], suggesting that there is a constant interfacial shear strength with increasing contact pressure [20]. We confirmed the linear scaling of friction with load from Ref. [24] in the current study. Figure 6a shows friction vs. load curves in two different environments. The first environment

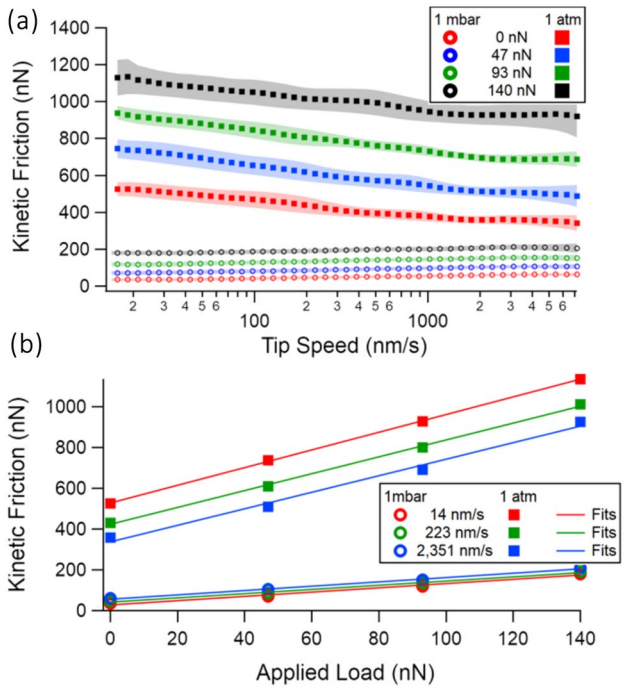

Fig. 6 **a** Friction vs speed curves for various applied loads. The four applied loads are tested in 10%RH air and at reduced ambient pressure. **b** Friction vs load curves generated from the data in (**a**), for both sliding environments. The curves are captured at three different speeds, with similar trends. Linear fits are applied to each set of data

is 10%RH air. Unlike the results of Fig. 5, velocity-weakening is observed at all normal loads, suggesting the interfacial bonding has a dominant effect on the friction response. The second environment is a reduced pressure of 1 mbar. We expect, based on our results thus far, that interfacial bonding is greatly reduced in this low humidity environment, so Prandtl–Tomlinson velocity-strengthening dominates the friction magnitude and any effect of stress enhancement should be minimal. Similar to Fig. 2b at the same chamber pressure, velocity-strengthening is experimentally observed in Fig. 6a. The data in Fig. 6a is used to generate the friction vs. load curves shown in Fig. 6b. For each environment, we show data corresponding to three different sliding speeds. In all cases, reasonably good linear fits confirm approximately linear friction scaling with load. This suggests that any stress enhancement of interfacial bonding does not have a large effect in the load range of the study.

4 Multi-Bond Simulation Methods

4.1 Multi-Bond Model

To couple the humidity dependence observed in the experiments with specific tribochemical reaction pathways, we carried out a series of multi-bond simulations [73]. A multi-bond model approximates the overall frictional response of a sliding interface as the result of interactions originating from a collection of fictitious "bonds" connecting the tip and the substrate. The dynamics of a tip laterally moving on a substrate is described by the following one-dimensional equation of motion [73],

$$M\ddot{X} + \eta\dot{X} + K(X - Vt) + F_b = 0 \tag{4}$$

where M is the effective mass of the AFM tip, η is the damping coefficient, K is the lateral stiffness of the AFM cantilever, X is the position of the tip, V is the sliding velocity of the tip, t is time, F_b is the force exerted to the tip due to the interfacial "bonds". The nature of the "bonds" can be varied based on the target system being studied. For example, F_b can represent the force originated from the capillary water bridge formed at each single-asperity contact across the multi-asperity interface [74], from stretching interfacial chemical bonds [75] formed within the single-asperity contact [70, 76], or from atomistic wear events [77]. The total kinetic friction is calculated as the time average of the instantaneous lateral force on the tip $F = -K(X - Vt)$.

4.2 Activation-Passivation Loop (APL) Model

We previously built a multi-bond model specifically for a silica-silica interface [26], where the ICBI friction was simulated by explicitly considering the formation and rupturing of interfacial siloxane bonds (Si–O–Si) across the tip-substrate interface. This was done by assuming $F_b = \sum_{i=1}^{N} f_c^i$, where N is the number of interfacial siloxane bonds and f_c^i is the friction force applied to the tip to stretch the i^{th} bond during the tip sliding. Equation (4) is solved numerically with a finite time step that is small enough to capture the kinetics of bond formation and bond-breaking. At every time step, the bonding state at each reaction site within the contact, either formed or ruptured, is updated stochastically according to the activation energies assigned locally for the corresponding chemical reactions.

More specifically, in this model [26], a surface reaction site can either be in "bonded state (BS)", "dangling state (DS)", or "passivated state (PS)" during sliding. For silica-silica interfaces, the PS site represents the silanol group (Si–OH) on the hydroxylated silica surfaces [78, 79]. This PS site can react with the opposing surface, and therefore be "activated", and form an interfacial siloxane bond (Si–O–Si) to become a BS site [21–23, 80]. The BS site is equivalent to the interfacial bond state (IBS) site in our newly modified model that will be introduced in the following section. The BS site is connected with the opposing surface with a fictitious spring, which results in the bonding friction f_c, while

the tip is laterally translated. The interfacial bond will eventually break due to the stretching of the bond and become a DS site. The DS site is highly reactive and can either reform an interfacial bond and become a BS site or be passivated by water molecules and form a PS site again. Therefore, these three states, i.e., BS, DS, and PS states, form a closed chemical reaction loop, prompting the designation of the multi-bond model as the "activation-passivation loop" (APL) model. In the APL model, we demonstrated that such a chemical reaction loop alone can lead to the logarithmically velocity-weakening frictional response, a phenomenon described as the evolution effect in phenomenological RSF models. Our past work suggested that the "state" of a contact can have a chemical origin, with the evolution of the state attributed to changes in the number of interfacial chemical bonds as the sliding velocity varies. In addition, the memory distance, Dc, can be interpreted within our model as the sliding distance required to passivate a dangling bond via interaction with a water molecule. Further discussions about the memory distance in ICBI friction can be found in our earlier work [26].

4.3 Humidity-Dependent Activation-Passivation Loop (HD-APL) Model—Chemical Loop

Here, we further develop our APL model by incorporating two different humidity dependencies on the surface chemistries: (1) the catalytic effect of water molecules on the interfacial chemical bonding and breaking reactions [34, 81–84], and (2) the lubrication effect from forming a thick water layer at a higher humidity level [34, 69, 85, 86].

In order to simulate the catalytic effect of water molecules, the activation energy for bond formation and bond-breaking is lowered when water molecules are present at the reaction sites in accordance with earlier theoretical studies [34, 81]. We also introduce a new state, which is called a "surface bond state (SBS)", representing a non-reactive in-plane surface siloxane bond (Si–O–Si) [83]. The bonded state (BS) in the original model is replaced by interfacial bond state (IBS) in order to distinguish it from SBS. The SBS site is necessary in our model to simulate the humidity-dependent number of silanol groups (or equivalently PS sites) on the silica surface at equilibrium [31, 82, 83, 87], i.e., a higher surface density of surface silanol groups is expected at a higher humidity level. This is achieved in our model by allowing the SBS site to be reactivated by water molecules and thereby to transform to a PS site. The new chemical loop formed among the four chemical states, i.e., IBS, SBS, DS, and PS states, is shown schematically in Fig. 7.

As shown in Fig. 7, each chemical process is assigned an activation energy. The activation energies colored in red correspond to the "dry" process (i.e., without water molecules participating), and the activation energies colored in blue correspond to the "wet" process (i.e., with water molecules involved in the reaction). For example, a PS site can form a bond via either a "dry" or "wet" process [34], and the activation energies for each of these processes, respectively, are denoted as E_{a1}, and $E_{a1,water}$. The same naming scheme is used for bond-breaking processes as well [81], i.e., E_{a2} and $E_{a2,water}$ refer to the activation energies of "dry" (from IBS to DS) and "wet" (from IBS to PS) bond-breaking processes, respectively. Dangling bonds can also participate in different types of reactions; E_{a3} represents the activation energy for a dangling bond to reform either an interfacial siloxane bond (IBS) or a

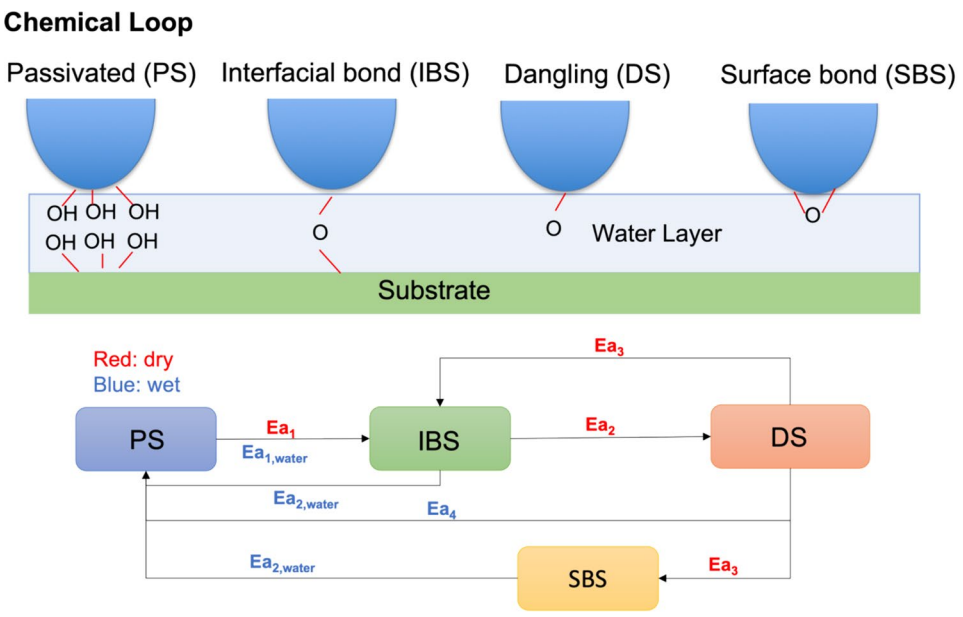

Fig. 7 Schematic plot of the chemical loop in our humidity-dependent activation-passivation loop model. The reaction site can be converted to a different surface state during tip sliding with different activation energies. The activation energy for "dry" and "wet" processes is colored in red and blue, respectively

surface siloxane bond (SBS), and E_{a4} is the barrier for passivating a dangling bond (PS).

The activation energies mentioned above determine the reaction rate Γ via the following equations,

$$\Gamma_{fic} = w_{fic}\exp\left(-E_{a,fic}/k_BT\right) \tag{5}$$

$$\Gamma_{fdc} = w_{fdc}\exp\left(-E_{a,fdc}\left(1-f_c/f_{c\_crit}\right)^{2/3}/k_BT\right) \tag{6}$$

where k_B is the Boltzmann's constant, T is the temperature, and w's and E_a's are the attempt frequencies and the activation energies, respectively. The subscripts *fic* and *fdc*, respectively, represent force-independent and force-dependent chemical reactions. Among the chemical reactions shown in Fig. 7, only those bond-breaking reactions that mechanically stretch the interfacial bond, i.e., from IBS to PS and from IBS to DS, are described by Eq. (6). For all other reactions without a bond being stretched, such as formation of an interfacial bond (from PS to IBS) and hydroxylation of a surface siloxane bond (from SBS to PS), the reaction kinetics are described by Eq. (5).

In Eq. (6), $f_c = k_c\Delta x_c$ is the friction force due to stretching a single interfacial chemical bond at a given reaction site while the tip is laterally translated. Δx_c is the elongation distance of a single bond. k_c is the bond stiffness, determined by $k_c = f_{c\_crit}/\Delta x_{c\_crit}$, where f_{c_crit} and Δx_{c_crit} are the critical force and critical elongation distance for breaking a single bond, respectively. A chemical bond is forced to break when $f_c > f_{c\_crit}$, or equivalently when $\Delta x_c > \Delta x_{c\_crit}$. In the meantime, a chemical bond is also allowed to break due to thermal activation before being stretched to the critical elongation length, where the kinetics for such thermally activated bond-breaking process is described by Eq. (6). Here, we assume the 2/3 power law dependence of activation energy for bond rupture on the friction force, in accordance with the "ramped creep" condition [77, 88, 89], which was found to describe siloxane bond rupture in single-molecule force spectroscopy measurement quite well [90].

Whether a reaction proceeds via a wet process and is catalyzed by water molecules or a dry process without water molecules is determined stochastically at each simulation time step by the humid probability $0 < P < 1$. A higher humidity probability P in the simulations represents a higher % RH in the experiments, and thus, P can be seen as an implicit measure of the humidity level. Although it is possible to relate P to % RH by assuming a certain functional form of water adsorption isotherm (see further discussion in SI), this will inevitably introduce additional assumptions and fitting parameters. Here we choose not to explicitly assume any quantitative relationships between P and % RH. Instead, we report the simulation results as a function of P in the results section, under the assumption that there exists a monotonic relationship between P and % RH.

In addition to the catalytic effect of water molecules, it was also reported in both experiments and theoretical studies that a thick water layer at high humidity can act as a lubricant [69, 85] and that a full monolayer of water molecules at the interface is enough to separate the surfaces and preclude interfacial bonding [34, 86]. This effect is implemented in our model by multiplying the reaction rate constant for the interfacial bonding process (from a PS to a IBS) by a penalty function that monotonically decays with increasing humid probability P. Specifically, the penalty function takes the form of a sigmoid function $1/\left(1+e^{\beta}\right)$, where $\beta = a\left(P-P_0\right)$. The reaction rate constant for interfacial chemical bond formation, i.e., Γ_{fic} as described by Eq. (5), is multiplied by the penalty function, only in cases when the reaction site is considered to be "wet" at a given time step. In other words, the chemical bond formation reaction at a "dry" reaction site will not be affected by any water molecules present at other "wet" reaction sites.

In the penalty function, a and P_0 determine how fast the reaction rate for interfacial bond formation decays with increasing P, which affects the relative contributions of the binding and intrinsic friction to the total kinetic friction. In the simulation results shown below, we set $a = 30$ and $P_0 = 0.5$, which can capture the substantial decrease in the rate of interfacial chemical reactions when there is a large number of interfacial water molecules present [86], and reproduce the trends observed in our humidity-dependent experiments (Fig. 3b) reasonably well. We also performed simulations with other values of a and P_0, which is presented in the SI section. These simulations show worse agreements with the experimental observations due to the penalty to the bond formation reaction rate constant being too strong or too weak.

4.4 Humidity-Dependent Activation-Passivation Loop (HD-APL) Model—Mechanical Loop

Recent studies demonstrated that when there are two types of contacts with distinct activation energies for contact formation, the velocity-dependence of the kinetic friction shows double-peak behavior, and thus, the transition from the velocity-weakening to velocity-strengthening kinetic friction occurs as the sliding velocity increases [70, 76]. This is because the formation of stronger contacts with higher activation energy for contact formation will be kinetically suppressed as the sliding velocity increases, while the weakly activated process with lower activation energy for contact formation will dominate the frictional interactions at higher sliding velocity.

In the silica-silica interface, the interfacial siloxane bonds are responsible for the strong covalent interaction that leads to velocity-weakening behavior at a sliding interface [26], which is already incorporated in our model via the chemical loop introduced above. Here, in order to simulate the velocity-strengthening trend observed in our experiments (see Fig. 3b), we introduce a second type of friction induced by the intrinsic surface energy corrugation, which represents the weakly activated process that should dominate the frictional response in the high velocity regime. We call such friction "intrinsic friction", as it describes the universal interactions which exist at all solid–solid interfaces, although such friction can be negligible in the case of superlubrication [91, 92]. Our experimental results shown in Fig. 3b clearly indicates that there is a finite friction even when the interfacial chemical bonding is greatly suppressed at the lowest (1% RH) and the highest (60% RH) humidity levels. Therefore, we will assume a non-zero contribution from such intrinsic noncovalent interaction between the tip and the substrate in our model.

The intrinsic friction is introduced in our model via the so-called mechanical loop. In the mechanical loop, the entire tip is either in the "stick state (StS)" or the "slip state (SlS)". In the StS, the tip is connected to the substrate with a single fictitious spring, whose spring constant is different from that of an interfacial chemical bond (IBS) in the chemical loop. The spring breaks when the tip slips, and then, the state of the tip transitions to the SlS. This mechanical loop resembles the thermally activated Prandtl–Tomlinson (PTT) model-type friction, where the tip hops from one local energy minima to the other along a corrugated potential energy surface with the aid of thermal activation. Consequently, we set a 0 eV barrier for the transition from the SlS to StS, but a finite activation energy E_{a5} for the inverse process. The mechanical loop is depicted schematically in Fig. 8.

Our silica-silica interface is amorphous, and the surface energy landscape should be random in nature. However, it was previously derived that the average frictional response of a non-aging amorphous interface can be described by the PTT model with an average activation barrier for hopping [93], under the assumption that the apparently smooth sliding observed could actually be irregular stick–slip with different local activation energy for the slip at different locations [94]. In our model, we approximate the intrinsic friction due to the tip-substrate energy corrugation using a single activation energy E_{a5}, which should represent the average energy corrugation across the interface.

Similar to the chemical loop, we describe the transition from StS to SlS as a thermally activated process, and thus, the transition rate is calculated by the following equation,

$$\Gamma_m = w_m \exp\left(-E_{a,m}\left(1 - f_m/f_{m\_crit}\right)^{2/3}/k_B T\right) \quad (7)$$

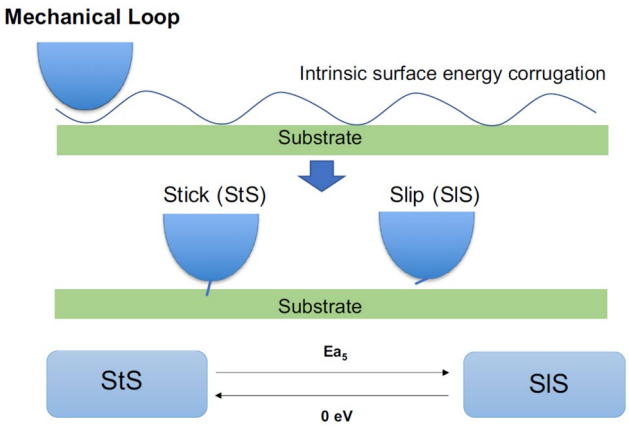

Fig. 8 Schematic plot of the mechanical loop in our humidity-dependent activation-passivation loop model. The tip-substrate contact from the intrinsic surface energy corrugation is simplified with a single fictitious spring with 0 eV barrier for formation but a finite barrier Ea_5 for breaking

where the subscript m indicates that the process is within the mechanical loop. In our model shown in Fig. 8, there is only one process that has a finite activation energy E_{a5}, and therefore, $E_{a,m} = E_{a5}$. The same 2/3 power law is assumed here, which has been analytically derived for thermally activated PTT model [88, 95].

As we consider the lubrication effect of the water layer in the chemical loop, we also assume that the intrinsic friction is lowered at a high humidity level [69, 85]. This effect is implemented by setting the activation energy E_{a5} to linearly decrease with increasing humid probability P, such that $E_{a,m}$ and f_{m_crit} are half of the original value at the highest value of $P = 1$. Here, $E_{a,m}$ is assumed to decrease proportionally with f_{m_crit} in accordance with the PTT model. [95] We did not let the values of $E_{a,m}$ and f_{m_crit} reach zero at the highest humidity probability P, based on our experimental observation (see Fig. 3b) that there is still finite friction that increases with sliding velocity even at the highest humidity level (60% RH), when the ICBI friction should be greatly suppressed.

Note that it was also reported that friction can be an increasing function of humidity due to surface-specific mechanisms, such as the registry of water molecules at the interface [69] and the formation of a meniscus around the tip-sample contact [96]. These effects are ignored in our model based on the observations obtained from our experiments. Specifically, we observe a non-monotonic dependence of friction on humidity (see Fig. 3b). As discussed earlier in this paper, we hypothesize that the interfacial chemical bonding occurs in the middle range of humidity levels, but only a limited amount of chemical bonding occurs at the lowest (1%) and highest (60%) humidity. Also, as shown in Fig. 3b, kinetic friction at the lowest humidity

(1%) is much higher than the friction at the highest humidity (60% RH). Therefore, it is reasonable to assume that the main role of a thick water layer is to act as a lubricant layer to reduce the friction due to the intrinsic surface energy corrugation. In fact, if we introduce the non-monotonicity in the dependence of E_{a5} on humid probability P, the overall non-monotonic dependence of friction on humidity will become more pronounced in the simulation. However, as we will show below, such non-monotonic dependence of intrinsic friction on humidity is not necessary for reproducing the non-monotonic humidity dependence of kinetic friction observed in the experiments.

As described above, in our current model, there are two independent types of tip-substrate interactions, i.e., bonding friction and intrinsic friction. Therefore, the total tip-substrate interaction F_b appearing in Eq. (4) is now the sum of two independent interfacial interactions, i.e.,$F_b = \sum_{i=1}^{N} f_{c\_i} + f_m$, where the values of f_{c_i} and f_m are the friction forces from the individual interfacial bond and the intrinsic surface energy corrugation, respectively. The values of f_{c_i} and f_m are determined by micro kinetic processes in chemical (Fig. 7) and mechanical loops (Fig. 8), respectively, at each simulation time step.

4.5 Simulation Parameters

For each reaction site, we assign activation energies (E_{a1},E_{a2},…E_{a5}) for all processes represented in the chemical and mechanical loops shown in Fig. 7 and Fig. 8. The activation energies in the chemical loop are sampled from Gaussian distributions rather than assigned a fixed value to account for the heterogeneity of the reaction sites and their geometries on amorphous surfaces [23]. The activation energy distributions used in our simulation are shown in Fig. 9, and the justifications for the mean values and the standard deviations are given below.

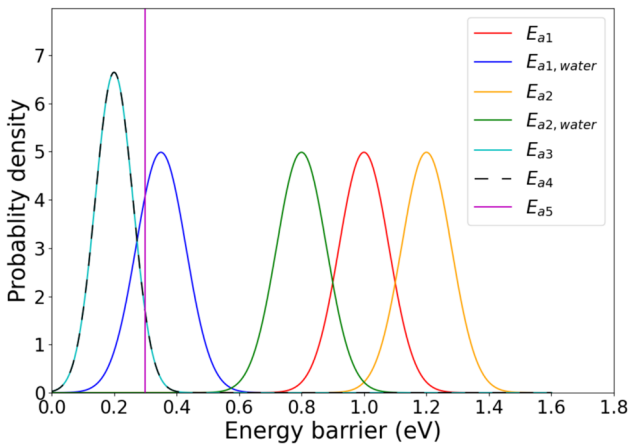

Fig. 9 Activation energy distributions used in the simulations. All the distributions are Gaussian, except for E_{a5} which is a delta function

In order to include the catalytic effect of water molecules on chemical bond formation [34] and breaking [81], we set the parameters in such a way that $\overline{E}_{a1,\text{water}} < \overline{E}_{a1}$ and $\overline{E}_{a2,\text{water}} < \overline{E}_{a2}$, where $\overline{\cdots}$ means the average value for all reaction sites at the interface. More specifically, the values of $\overline{E}_{a1}$ and $\overline{E}_{a1,\text{water}}$ for siloxane bond formation are set to 1.0 and 0.35 eV, respectively. These values agree with the DFT calculation results shown in Fig. 1 [34], where the activation energies to bond formation with and without water are 25.6 kcal/mol (1.1 eV) and 7.1 kcal/mol (0.31 eV), respectively. For the bond-breaking process, we chose $\overline{E}_{a1} = 1.2$ eV for the dry process, which is based on the *ab initio* Molecular Dynamics simulation results (~ 100–125 kJ/mol) for stretching siloxane elastomers. For water-catalyzed siloxane breaking process, we chose the value $\overline{E}_{a1,\text{water}} = 0.8$ eV, which is within the range of the values reported by previous ab initio methods (0.32–1.27 eV) [81, 97].

The standard deviation of the distributions of activation energies of E_{a1}, $E_{a1,\text{water}}$, E_{a2}, and $E_{a1,\text{water}}$ is chosen to be 0.08 eV. The resulting range of activation energy E_{a1} (~ 0.76–1.24 eV) is consistent with our previous kinetic Monte Carlo simulation work, where the experimental contact ageing results for silica-silica interface is reproduced [29]. The lower bound of E_{a1} is set to ~ 0.8 eV, which is identified to be an important feature to achieve linear contact ageing behavior observed experimentally at short time scale (< 0.1 s) [54]. Here, in order to reduce the number of parameters, we assume the same width of activation energy distribution for $E_{a1,\text{water}}$, E_{a2}, and $E_{a1,\text{water}}$.

For the chemical processes involving dangling bonds, we chose the lowest activation energy among all processes to account for the highly reactive nature of a dangling bond, i.e., $\overline{E}_{a3} = \overline{E}_{a4} = 0.2$ eV, with a standard deviation of 0.06 eV. These values are the same as what we used in our original APL multi-bond model simulation [26].

Finally, for the intrinsic friction in the mechanical loop, we assign a single value for the activation energy $E_{a5} =$ 0.3 eV, assuming that the heterogenous surface corrugation is averaged out across the interface and that the silica surface is overall relatively flat without a large change in the energy corrugation during sliding [98]. A relatively lower value, compared to the siloxane bond-breaking processes (E_{a2} and $E_{a2,\text{water}}$), is assigned to represent the weaker noncovalent nature of such intrinsic friction [88].

We will report the friction force normalized by the contact area, which has the same units as shear stress, instead of the absolute frictional values. No explicit assumptions are made based on the single-asperity or multi-asperity contact (such as Hertzian contact pressure distribution, or the load-dependence of the real contact area). Our previous experimental and theoretical works on contact ageing

at silica-silica interface in either single-asperity [24, 29] or multi-asperity [28] contact showed that the total friction is approximately a linear function of the real contact area if the contact pressure is relatively low. This is because the total friction linearly scales with the number of interfacial siloxane bonds, and the number of interfacial bonds, in turn, increases linearly with the real contact area at a constant surface density of silanol groups. The typical surface density of silanol groups on a fully hydroxylated amorphous silica surface was experimentally measured to be around $\rho_{OH} = 4\ nm^{-2}$ [78], which is the value set to be the maximum surface density of silanol groups in our computational model. Since all experiments except the load-dependent tests shown in Figs. 5and 6 were conducted at a low constant applied load (0 nN) and an estimation of the exact contact area at the sliding interfaces is challenging, we report the friction force normalized by the contact area instead of the absolute frictional values, aiming to qualitatively compare the agreement between the experimental and simulation results.

As we mentioned in the experimental section, we will also ignore the capillary effect on the change in the real contact area. Such an assumption is based on our experimental results showing that (see the inset of Fig. 3a) there is no obvious correlation between adhesion and the ageing response ΔF within the middle range of humidity levels (10–40% RH). Thus, in our model, we assume that the change in adhesion force in our experiment is not large enough to induce a significant change in the real contact area of our silica-silica interface.

In addition, we also do not explicitly include the normal pressure dependence on the activation energies [29, 70, 76, 99] in our current model. This assumption is validated by our experimental results shown in and discussed for Fig. 6.

Other parameters used in our simulations are as follows. Most are chosen based on the estimations from experiments, but some are derived from theoretical predictions: $w_{c1} = w_{c2} = 10^{13}$ Hz (a typical atomic vibrational frequency is ~ $10^{12–13}$ Hz), $w_m = 10^6$ Hz (a typical AFM tip slip attempt frequency is ~ $10^{4–6}$ Hz) [52, 95], $f_{c\_crit} = 3.0$ nN (experimentally measured critical siloxane bond rupture force is ~ 2.9 nN) [90], $\Delta x_{c\_crit} = 0.2$ nm (maximum bond elongation of a siloxane bond before rupturing is ~ 0.2 nm according to the ab initio MD simulation), [100] $f_{m\_crit} = 1.5\ nN/nm^2$ (an estimation obtained from the AFM experimental measurement that shows critical friction force of ~ 1–1.5 nN for a contact area of ~ 1–10 nm^2) [52, 95], $\Delta x_{m\_crit} = 1.0$ nm (a typical periodicity of surface energy landscape estimated from the AFM experiment is ~ 0.1–1.0 nm) [52, 95], $\Delta t = 2 \times 10^{-9}$ s (a small enough simulation time step for describing various types of chemical reactions), $M = 10^{-11}$ kg (an estimation based on the AFM experiment) [52], $\eta = 4 \times 10^{-4}$ kg/s (the smallest damping coefficient considered in our previous model) [26], and $K = 20$ N/m (determined from the experimental lateral force calibration). All the simulation results are obtained by averaging over a sliding distance of at least 100 nm.

4.6 Multi-bond Simulation Results

The simulation results of our HD-APL multi-bond model are shown in Fig. 10. The sliding velocity dependences of the total kinetic friction, as well as the two major contributions to the total kinetic friction, i.e., the bonding friction and the intrinsic friction, at different humidity probabilities *P*s are shown in Fig. 10a, b, c, respectively. From Fig. 10a, we can observe two qualitative trends that agree with experimental results shown in Fig. 3b: (1) the friction force depends nonmonotonically on humidity, and (2) there are transitions from velocity-strengthening to -weakening, and finally to -strengthening again, as the humidity increases.

The non-monotonic humidity dependence results in peak friction values appearing at the humidity probability $P = 0.5$, as shown in Fig. 10a. Examining the humidity dependence of the bonding friction and the intrinsic friction shown in Fig. 10b and c, it becomes evident that such non-monotonic humidity dependence of the total kinetic friction is solely attributed to the contribution of chemical bonding alone, whereas the intrinsic friction decreases monotonically with increasing humidity. The non-monotonic contribution from bonding friction is due to the two competing effects from the water molecules [34] implemented in our model, which can (1) either promote interfacial chemical bonding by generating a larger number of reactive surface silanol groups and reducing the bonding energetics, or (2) preclude interfacial chemical bonding by separating the surfaces due to the presence of a thick water layer. In the previously reported experiments [21, 60, 61], the highest friction values are obtained in the range of 5–20% RH. At the same time, it was also reported that on silica, a full monolayer of water molecules can be obtained around 10% RH [101]. Assuming that a similar water layer thickness remains at the sliding interface, both our simulation and experimental results show that the highest friction is obtained for the interfaces that are considerably wet. Hence, our simulation results indicate the importance of water molecules in activating the interfacial chemical bonding at silica-silica interface.

The second trend, i.e., the transitions in the velocity-dependence of friction as humidity increases, is also observed in our simulation results as show in Fig. 10a. According to our simulation results, the bonding friction is always velocity-weakening (see Fig. 10b), whereas the intrinsic friction is always velocity-strengthening (see Fig. 10c). The transition occurs because the relative contributions from velocity-weakening bonding friction (Fig. 10b) and velocity-strengthening intrinsic friction (Fig. 10c) change as the humidity probability *P* increases. Specifically, both at low ($P <= 0.1$) and high ($P >= 0.9$) humidities, the

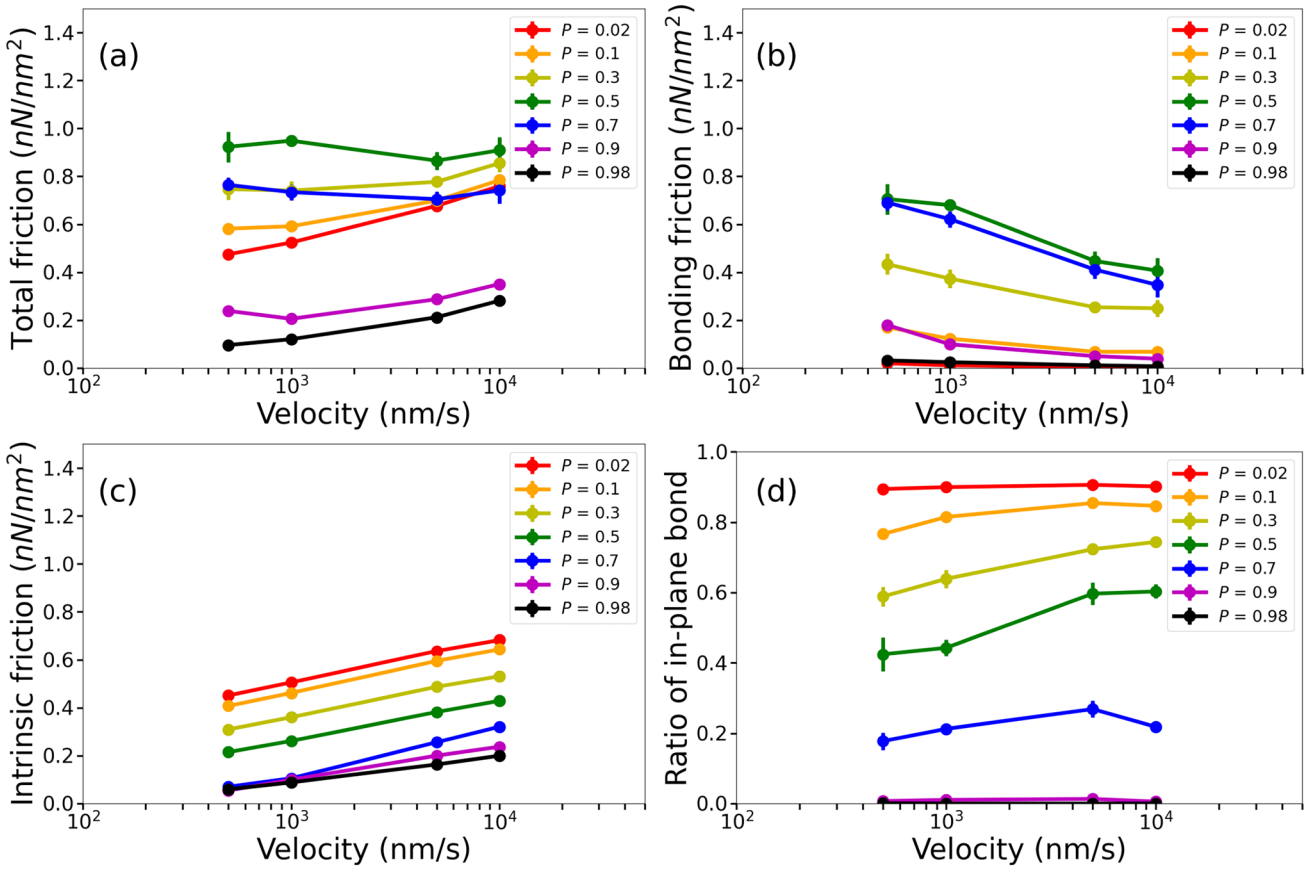

Fig. 10 Multi-bond simulation results. **a–c** Velocity and humidity dependence of total, bonding, and intrinsic friction per unit contact area. The error bar represents the standard deviation from the five independent simulations with different random seeds. **d** Ratio of in-plane siloxane bonds (SBS sites) to the total number of reaction sites as a function of sliding velocity at different humidity levels. The velocity on the x axis is shown in logarithmic scale

bonding friction is greatly suppressed. As a result, the total friction is dominated by the intrinsic friction, showing a strong velocity-strengthening trend. In contrast, in the intermediate humidities ($0.3 <= P <= 0.7$), the bonding friction becomes much higher, and the velocity-strengthening trend gradually transitions to velocity-weakening. The velocity-weakening in Fig. 10a is most pronounced at $P = 0.7$, where the friction decreased from 0.76 to 0.7 nN/nm^2 (~8% decrease) within the velocity range of 500–5000 nm/s. Also, at $P = 0.5$, the friction decreased from 0.92 to 0.87 nN/nm^2 (~5% decrease) within the velocity range of 500–5000 nm/s. For comparison, in Fig. 3b, the experimentally measured friction decreases from ~200 to ~180 nN (~10% decrease) within the same velocity range. Although exact agreement between our simulations and experiments is not obtained regarding the degree of velocity-weakening, our model captures the two major qualitative trends observed in our experiments, i.e., the non-monotonic humidity dependence of kinetic friction and the transitions in the velocity-dependence of kinetic friction as humidity increases. As we did not globally fit our model to the experimental data, and the simulation parameters are selected to be physically justifiable (see Simulation parameters section for the detailed justification of simulation parameters), we regard such agreements on the qualitative trends as noteworthy, affirming the validity of the surface chemistry-related assumptions in our computational model.

Interestingly, the simulation results show a considerably stronger velocity-strengthening effect at the lowest ($P = 0.02$) and the highest ($P = 0.98$) humidity probability than the experiments at 1 and 60% RH. One possible reason for the less significant velocity-strengthening effect in experiments is that there is still a small amount of ageing occurring at 1 and 60% RH, as detected in SHS experiments shown in Fig. 3a. In contrast, interfacial chemical bonding is highly suppressed in extremely dry ($P = 0.02$) and wet ($P = 0.98$) conditions in the simulations, resulting in the near-zero bonding friction at these humidities, as shown in Fig. 10b. The small amount of ageing observed in the experiments implies that the velocity-strengthening effect from the intrinsic friction can be partially compensated by the velocity-weakening effect from the bonding friction, and

thus, the overall velocity-strengthening trend is less significant than what simulations show.

Our simulation results further indicate that the reasons for the low values of bonding friction at these two extreme humidity probabilities are different. At $P = 0.02$, the low value of bonding friction arises because most of the reaction sites are stabilized at SBS (in-plane siloxane bond), which are non-reactive and do not form interfacial chemical bonds during sliding. In Fig. 10d, the ratio of SBS sites (in-plane Si–O–Si groups) to the total number of reaction sites are plotted as a function of velocity at different humidity probabilities. As it can be seen, during sliding at $P = 0.02$ most of the reaction sites are of the SBS type, and thus, do not directly participate in the interfacial chemical bonding reactions. This is not the case at $P = 0.98$, where most of the SBS sites have been activated by the hydrolysis reaction and became reactive PS sites. The reactive PS sites are readily available for interfacial bond formation, and therefore, a surface with more PS sites can potentially form more interfacial chemical bonds and have a higher bonding friction. However, due to lubrication effect of a thick water layer, the reaction kinetics for bond formation is substantially reduced at the highest humidity probability. As a result, our model predicts a significantly low bonding friction at $P = 0.98$ as shown in Fig. 10b. Therefore, our simulation results confirm the experimental results that the interfacial chemical bonding contributes to the friction only within intermediate humidity levels. The humidity level should be high enough to promote the interfacial bonding reaction kinetics, but should not be too high to physically separate the reacting surfaces and preclude the interfacial chemical bonding.

5 Discussion

The variation of friction response with relative humidity on hydrophilic surfaces like the plasma-cleaned SiO_2 examined here has had a substantial history of study. In many cases [58, 96, 102, 103], the response has been attributed to the dynamics of capillary formation and motion, rather than the interfacial bonding mechanism proposed here and in earlier work. In Chen et al. [96], for instance, a similar trend of velocity-weakening friction with increasing humidity in an SiO_2–SiO_2 contact is observed. This is attributed to the influence of a capillary whose inferred size varies with the sliding speed. Szoszkiewicz and Riedo [102] reach similar conclusions in the context of a multi-asperity context, but in that case the speed-dependence was attributed to the *number* of capillaries formed at nanoasperities within the nominal contact area. Such nanocapillaries are assumed to be immobile and break after some small translation of the contact; hence new capillaries must be formed continuously, leading to a speed-dependent steady-state population. Empirical measurements of the size behavior of capillaries via adhesion reach different conclusions, however. In Cassin et al. [104], an AFM tip hovering over an SiO_2 sample surface could detect the formation of a capillary via a change in normal force on the tip. It was found that, indeed, capillary formation was a thermally activated Arrhenius process, but that after the size of the capillary grew from the initial nucleation volume to the equilibrium volume, this volume remained constant for all speeds below 100 um/s. It also showed that, once formed, the capillaries were persistent and could translate with the tip. Noel et al.[105], by measuring the pulloff force of an AFM probe while sliding, found a maximum speed of at least 10 um/s before capillary size (or in the multi-asperity picture, the nanocapillary population) began to vary. At higher speeds, Noel et al. attributed the size variation to an activation barrier for capillary growth, rather than nucleation as Chen et al. concluded, which was influenced by local surface inhomogeneities in chemistry and morphology. Inhomogeneities that raise this local activation barrier were expected to be encountered more frequently at higher sliding speeds. Since our results show strong velocity-weakening at speeds as slow as 3 nm/s, variation in capillary size cannot explain the velocity-weakening. Additionally, the load-dependent friction in Fig. 5 shows a change from velocity-strengthening to velocity-weakening with increasing load. In the context of the capillary explanations, the capillary size dependence on the load should be small and velocity-weakening should be observed at all loads. Our ageing trends in Figs. 2a and 3a cannot be due to capillary growth since in Cassin et al. it was found this process was complete within 10 ms, much faster than ageing times as long as 100 s used in this study. Nucleation times were similarly short in Cassin et al.'s study.

Additionally, a different study with heated AFM probes in similar nanoscale SiO_2–SiO_2 contacts observed strong velocity-weakening even at high temperatures that preclude the presence of a capillary meniscus [61].

In Chen et al. [96], they also observe a monotonic increase in kinetic friction with increasing %RH while the present study shows non-monotonic friction. This can be rationalized by noting that Chen et al., among other differences, performed their experiments at a higher average contact pressure of 1 GPa than the present study with zero applied load and an average contact pressure at high %RH in the range of 700 MPa (although there is uncertainty in this value given the apparent multi-asperity friction-load scaling discussed earlier). Therefore, it is possible the local pressures were sufficient in Chen et al. to displace the ice-like water layer and eliminate the non-monoticity in friction vs. %RH seen in the current study.

6 Conclusions

We have shown that amorphous SiO_2–SiO_2 contacts can exhibit a prototypical RSF response in ageing as well as velocity-dependent kinetic friction. This response is modulated profoundly by the environmental humidity level. At the lowest humidities, ageing was nearly non-existent and the velocity-dependence was velocity-strengthening, which we attribute to a lack of interfacial bonding. At intermediate humidities, ageing was significant, and the velocity-dependence was velocity-weakening across the entire velocity range examined. Both of these effects are attributed to water-assisted interfacial chemical bonding across the interface. At the highest humidities, the amount of ageing was again reduced, and the velocity-dependence became velocity-strengthening again. This was attributed to a water layer separating the two counterfaces, which was supported by experiments showing that increasing the applied normal load could squeeze water out of the contact and reimpose a velocity-weakening regime.

Multi-bond simulations were performed to test scientific hypotheses regarding physical phenomena responsible for the friction trends observed in our experiments. Simulations incorporated humidity-dependent activation barriers for interfacial chemical bonds and an intrinsic surface energy corrugation. These simulations reproduced the general trends in humidity- and velocity-dependent friction observed in the experiments. These trends include the non-monotonic humidity dependence of kinetic friction at a given sliding velocity, and the transition from velocity-strengthening to velocity-weakening friction, and then back to velocity-strengthening friction, as humidity increases. The experimental agreement supports the validity of hypotheses that underly the physics of these simulations, namely (1) the catalytic effect of water molecules on interfacial chemical bonding reactions, and (2) a lubrication effect from a thick interfacial water layer at high humidities that prevents interfacial chemical reactions and reduces intrinsic non-bonding friction.

Our results demonstrate the importance of water to the friction response at the asperity level in the silica-silica system, and as such are relevant to understanding the tribological response of systems ranging from earthquake faults to microelectromechanical systems.

Supplementary Information The online version contains supplementary material available at https://doi.org/10.1007/s11249-024-01904-x.

Author Contributions JBM designed and performed all experiments. ZL and KB designed and performed all simulations. JBM and ZL wrote the manuscript. RWC and DG helped design and performed oversight of the experiments and manuscript preparation. IS helped design and performed oversight of the simulations and manuscript preparation.

Funding This work was supported by the NSF under Grant GEO-1951462 (RWC, DG, and JBM) and GEO-1951314 (IS and ZL). Some of the experimental work was carried out in part at the Singh Center for Nanotechnology, which is supported by the NSF National Nanotechnology Coordinated Infrastructure Program under Grant NNCI-2025608.

Data Availability All experimental and simulation data captured in preparation of this manuscript is available by request from the corresponding author.

Declarations

Conflict of interest The authors have no conflicts of interest to declare.

References

1. Marone, C.: Laboratory-derived friction laws and their application to seismic faulting. Annu. Rev. Earth Planet. Sci. **26**, 643–696 (1998). https://doi.org/10.1146/annurev.earth.26.1.643
2. Baumberger, T., Caroli, C.: Solid friction from stick–slip down to pinning and aging. Adv. Phys. **55**, 279–348 (2006). https://doi.org/10.1080/00018730600732186
3. Rabinowicz, E.: The nature of the static and kinetic coefficients of friction. J. Appl. Phys. **22**, 1373–1379 (1951). https://doi.org/10.1063/1.1699869
4. Baumberger, T., Heslot, F., Perrin, B.: Crossover from creep to inertial motion in friction dynamics. Nature **367**, 544–546 (1994). https://doi.org/10.1038/367544a0
5. Bar-Sinai, Y., Aldam, M., Spatschek, R., Brener, E.A., Bouchbinder, E.: Spatiotemporal dynamics of frictional systems: The interplay of interfacial friction and bulk elasticity. arXiv:1908.02820 [cond-mat, physics:physics] (2019)
6. Rabinowicz, E.: The intrinsic variables affecting the stick-slip process. Proc. Phys. Soc. **71**, 668 (1958). https://doi.org/10.1088/0370-1328/71/4/316
7. Rice, J.R., Ruina, A.L.: Stability of steady frictional slipping. J. Appl. Mech. **50**, 343–349 (1983). https://doi.org/10.1115/1.3167042
8. Morita, S., Fujisawa, S., Sugawara, Y.: Spatially quantized friction with a lattice periodicity. Surf. Sci. Rep. **23**, 1–41 (1996). https://doi.org/10.1016/0167-5729(95)00009-7
9. Dieterich, J.H.: Modeling of rock friction: 1. Experimental results and constitutive equations. J. Geophys. Res. **84**, 2161 (1979). https://doi.org/10.1029/JB084iB05p02161
10. Bhattacharya, P., Rubin, A.M., Beeler, N.M.: Does fault strengthening in laboratory rock friction experiments really depend primarily upon time and not slip? Is fault healing really time dependent? J. Geophys. Res. Solid Earth. **122**, 6389–6430 (2017). https://doi.org/10.1002/2017JB013936

11. Bhattacharya, P., Rubin, A.M., Tullis, T.E., Beeler, N.M., Okazaki, K.: The evolution of rock friction is more sensitive to slip than elapsed time, even at near-zero slip rates. Proc. Natl. Acad. Sci. U.S.A. **119**, e2119462119 (2022)
12. Ferdowsi, B., Rubin, A.M.: A granular-physics-based view of fault friction experiments. J. Geophys. Res.: Solid Earth. (2020). https://doi.org/10.1029/2019JB019016
13. Li, T., Rubin, A.M.: A microscopic model of rate and state friction evolution: microscopic model of friction evolution. J. Geophys. Res. Solid Earth. **122**, 6431–6453 (2017). https://doi.org/10.1002/2017JB013970
14. Ji, Y., Niemeijer, A., Baden, D., Yamashita, F., Xu, S., Hunfeld, L., Pijnenburg, R.P.J., Fukuyama, E., Spiers, C.: Friction law for earthquake nucleation: size doesn't matter (2022)
15. Li, S., Zhang, S., Chen, Z., Feng, X.-Q., Li, Q.: Length scale effect in frictional aging of silica contacts. Phys. Rev. Lett. **125**, 215502 (2020). https://doi.org/10.1103/PhysRevLett.125.215502
16. Dieterich, J.H., Kilgore, B.D.: Direct observation of frictional contacts: new insights for state-dependent properties. PAGEOPH. **143**, 283–302 (1994). https://doi.org/10.1007/BF00874332
17. Dillavou, S., Bar-Sinai, Y., Brenner, M.P., Rubinstein, S.M.: Beyond quality and quantity: spatial distribution of contact encodes frictional strength. Phys. Rev. E **106**, L033001 (2022). https://doi.org/10.1103/PhysRevE.106.L033001
18. Kilgore, B., Beeler, N.M., Lozos, J., Oglesby, D.: Rock friction under variable normal stress. J. Geophys. Res.: Solid Earth. **122**, 7042–7075 (2017). https://doi.org/10.1002/2017JB014049
19. Nagata, K., Nakatani, M., Yoshida, S.: Monitoring frictional strength with acoustic wave transmission. Geophys. Res. Lett. (2008). https://doi.org/10.1029/2007GL033146
20. Baumberger, T., Berthoud, P., Caroli, C.: Physical analysis of the state- and rate-dependent friction law. II: dynamic friction. Phys. Rev. B **60**, 3928–3939 (1999). https://doi.org/10.1103/PhysRevB.60.3928
21. Li, Q., Tullis, T.E., Goldsby, D., Carpick, R.W.: Frictional ageing from interfacial bonding and the origins of rate and state friction. Nature **480**, 233–236 (2011). https://doi.org/10.1038/nature10589
22. Vigil, G., Xu, Z., Steinberg, S., Israelachvili, J.: Interactions of Silica Surfaces. J. Colloid Interface Sci. **165**, 367–385 (1994). https://doi.org/10.1006/jcis.1994.1242
23. Liu, Y., Szlufarska, I.: Chemical origins of frictional aging. Phys. Rev. Lett. **109**, 186102 (2012). https://doi.org/10.1103/PhysRevLett.109.186102
24. Tian, K., Gosvami, N.N., Goldsby, D.L., Liu, Y., Szlufarska, I., Carpick, R.W.: Load and time dependence of interfacial chemical bond-induced friction at the nanoscale. Phys. Rev. Lett. **118**, 076103 (2017). https://doi.org/10.1103/PhysRevLett.118.076103
25. Tian, K., Gosvami, N.N., Goldsby, D.L., Carpick, R.W.: Stick-slip instabilities for interfacial chemical bond-induced friction at the nanoscale. J. Phys. Chem. B **122**, 991–999 (2018). https://doi.org/10.1021/acs.jpcb.7b09748
26. Tian, K., Li, Z., Gosvami, N.N., Goldsby, D.L., Szlufarska, I., Carpick, R.W.: Memory distance for interfacial chemical bond-induced friction at the nanoscale. ACS Nano (2019). https://doi.org/10.1021/acsnano.8b09714
27. Hatano, T.: Rate and state friction law as derived from atomistic processes at asperities. arXiv:1512.05078 [cond-mat, physics:physics]. (2015)
28. Li, Z.: Chemical aging of large-scale randomly rough frictional contacts. Phys. Rev. E (2018). https://doi.org/10.1103/PhysRevE.98.023001
29. Li, Z., Szlufarska, I.: Multiphysics model of chemical aging in frictional contacts. Phys. Rev. Mater. **2**, 063602 (2018). https://doi.org/10.1103/PhysRevMaterials.2.063602
30. Li, Z., Szlufarska, I.: Chemical creep and its effect on contact aging. ACS Mater. Lett. **4**, 1368–1373 (2022). https://doi.org/10.1021/acsmaterialslett.2c00356
31. Sneh, O., George, S.M.: Thermal stability of hydroxyl groups on a well-defined silica surface. J. Phys. Chem. **99**, 4639–4647 (1995). https://doi.org/10.1021/j100013a039
32. Sneh, O., Cameron, M.A., George, S.M.: Adsorption and desorption kinetics of H_2O on a fully hydroxylated SiO_2 surface. Surf. Sci. **364**, 61–78 (1996). https://doi.org/10.1016/0039-6028(96)00592-4
33. Koretsky, C.M., Sverjensky, D.A., Salisbury, J.W., D'Aria, D.M.: Detection of surface hydroxyl species on quartz, γ-alumina, and feldspars using diffuse reflectance infrared spectroscopy. Geochim. Cosmochim. Acta **61**, 2193–2210 (1997). https://doi.org/10.1016/S0016-7037(97)00056-2
34. Ootani, Y., Xu, J., Hatano, T., Kubo, M.: Contrasting roles of water at sliding interfaces between silicon-based materials: first-principles molecular dynamics sliding simulations. J. Phys. Chem. C **122**, 10459–10467 (2018). https://doi.org/10.1021/acs.jpcc.8b01953
35. Dieterich, J.H., Conrad, G.: Effect of humidity on time- and velocity-dependent friction in rocks. J. Geophys. Res.: Solid Earth. **89**, 4196–4202 (1984). https://doi.org/10.1029/JB089iB06p04196
36. Frye, K.M., Marone, C.: Effect of humidity on granular friction at room temperature. J. Geophys. Res.: Solid Earth. 107, ETG 11–1-ETG 11–13 (2002). https://doi.org/10.1029/2001JB000654
37. Beynon, S.J., Faulkner, D.R.: Dry, damp, or drenched? The effect of water saturation on the frictional properties of clay fault gouges. J. Struct. Geol. **140**, 104094 (2020). https://doi.org/10.1016/j.jsg.2020.104094
38. Morrow, C.A., Moore, D.E., Lockner, D.A.: The effect of mineral bond strength and adsorbed water on fault gouge frictional strength. Geophys. Res. Lett. **27**, 815–818 (2000). https://doi.org/10.1029/1999GL008401
39. Diao, Y., Espinosa-Marzal, R.M.: The role of water in fault lubrication. Nat. Commun. **9**, 2309 (2018). https://doi.org/10.1038/s41467-018-04782-9
40. Thom, C.A., Carpick, R.W., Goldsby, D.L.: Constraints on the physical mechanism of frictional aging from nanoindentation. Geophys. Res. Lett. **45**, 13306–13311 (2018). https://doi.org/10.1029/2018GL080561
41. Ootani, Y., Xu, J., Takahashi, N., Akagami, K., Sakaki, S., Wang, Y., Ozawa, N., Hatano, T., Adachi, K., Kubo, M.: Self-formed double tribolayers play collaborative roles in achieving superlow friction in an aqueous environment. J. Phys. Chem. C **124**, 8295–8303 (2020). https://doi.org/10.1021/acs.jpcc.0c02068
42. Ootani, Y., Xu, J., Adachi, K., Kubo, M.: First-principles molecular dynamics study of silicon-based ceramics: different tribochemical reaction mechanisms during the running-in period of silicon nitride and silicon carbide. J. Phys. Chem. C **124**, 20079–20089 (2020). https://doi.org/10.1021/acs.jpcc.0c04613
43. Chen, L., He, H., Wang, X., Kim, S.H., Qian, L.: Tribology of Si/SiO_2 in humid air: transition from severe chemical wear to wearless behavior at nanoscale. Langmuir **31**, 149–156 (2015). https://doi.org/10.1021/la504333j
44. Wang, X., Kim, S.H., Chen, C., Chen, L., He, H., Qian, L.: Humidity dependence of tribochemical wear of monocrystalline silicon. ACS Appl. Mater. Interfaces **7**, 14785–14792 (2015). https://doi.org/10.1021/acsami.5b03043
45. Williams, T.S., Hicks, R.F.: Aging mechanism of the native oxide on silicon (100) following atmospheric oxygen plasma cleaning.

J. Vacuum Sci. Technol. A. **29**, 041403 (2011). https://doi.org/10.1116/1.3597436
46. Sader, J.E., Chon, J.W.M., Mulvaney, P.: Calibration of rectangular atomic force microscope cantilevers. Rev. Sci. Instrum. **70**, 3967–3969 (1999). https://doi.org/10.1063/1.1150021
47. Li, Q., Kim, K.-S., Rydberg, A.: Lateral force calibration of an atomic force microscope with a diamagnetic levitation spring system. Rev. Sci. Instrum. **77**, 065105 (2006). https://doi.org/10.1063/1.2209953
48. Heslot, F., Baumberger, T., Perrin, B., Caroli, B., Caroli, C.: Creep, stick-slip, and dry-friction dynamics: experiments and a heuristic model. Phys. Rev. E **49**, 4973–4988 (1994). https://doi.org/10.1103/PhysRevE.49.4973
49. Villarrubia, J.S.: Algorithms for scanned probe microscope image simulation, surface reconstruction, and tip estimation. J. Res. Natl. Inst. Stand. Technol. **102**, 425 (1997). https://doi.org/10.6028/jres.102.030
50. Jansen, L., Hölscher, H., Fuchs, H., Schirmeisen, A.: Temperature dependence of atomic-scale stick-slip friction. Phys. Rev. Lett. **104**, 256101 (2010). https://doi.org/10.1103/PhysRevLett.104.256101
51. Petzold, C., Koch, M., Bennewitz, R.: Friction force microscopy of tribochemistry and interfacial ageing for the SiOx/Si/Au system. Beilstein J. Nanotechnol. **9**, 1647–1658 (2018). https://doi.org/10.3762/bjnano.9.157
52. Liu, X.-Z., Ye, Z., Dong, Y., Egberts, P., Carpick, R.W., Martini, A.: Dynamics of atomic stick-slip friction examined with atomic force microscopy and atomistic simulations at overlapping speeds. Phys. Rev. Lett. **114**, 146102 (2015). https://doi.org/10.1103/PhysRevLett.114.146102
53. Milne, Z.B., Hasz, K., McClimon, J.B., Castro, J., Carpick, R.W.: A modified multibond model for nanoscale static friction. Phil. Trans. R. Soc. A **380**, 20210342 (2022). https://doi.org/10.1098/rsta.2021.0342
54. Tian, K., Li, Z., Liu, Y., Gosvami, N.N., Goldsby, D.L., Szlufarska, I., Carpick, R.W.: Linear aging behavior at short timescales in nanoscale contacts. Phys. Rev. Lett. **124**, 026801 (2020). https://doi.org/10.1103/PhysRevLett.124.026801
55. Harrison, A.J., Corti, D.S., Beaudoin, S.P.: Capillary forces in nanoparticle adhesion: a review of AFM methods. Part. Sci. Technol. **33**, 526–538 (2015). https://doi.org/10.1080/02726351.2015.1045641
56. Asay, D.B., de Boer, M.P., Kim, S.H.: Equilibrium vapor adsorption and capillary force: exact laplace-young equation solution and circular approximation approaches. J. Adhes. Sci. Technol. **24**, 2363–2382 (2010). https://doi.org/10.1163/016942410X508271
57. Carpick, R., Batteas, J., Boer, M.: Scanning probe studies of nanoscale adhesion between solids in the presence of liquids and monolayer films. In: Bhushan, B. (ed.) Springer handbook of nanotechnology, pp. 951–980. Springer, Berlin, Heidelberg (2007)
58. Chen, L., Qian, L.: Role of interfacial water in adhesion, friction, and wear—a critical review. Friction. **9**, 1–28 (2021). https://doi.org/10.1007/s40544-020-0425-4
59. Xiao, C., Shi, P., Yan, W., Chen, L., Qian, L., Kim, S.H.: Thickness and structure of adsorbed water layer and effects on adhesion and friction at nanoasperity contact. Colloids and Interfaces. **3**, 55 (2019). https://doi.org/10.3390/colloids3030055
60. Greiner, C., Felts, J.R., Dai, Z., King, W.P., Carpick, R.W.: Controlling nanoscale friction through the competition between capillary adsorption and thermally activated sliding. ACS Nano **6**, 4305–4313 (2012). https://doi.org/10.1021/nn300869w
61. Greiner, C., Felts, J.R., Dai, Z., King, W.P., Carpick, R.W.: Local nanoscale heating modulates single-asperity friction. Nano Lett. **10**, 4640–4645 (2010). https://doi.org/10.1021/nl102809k
62. Kissinger, G., Kissinger, W.: Hydrophilicity of silicon wafers for direct bonding. Physica Status Solidi (A). **123**, 185–192 (1991). https://doi.org/10.1002/pssa.2211230117
63. Weeks, J.D.: Constitutive laws for high-velocity frictional sliding and their influence on stress drop during unstable slip. J. Geophys. Res.: Solid Earth. **98**, 17637–17648 (1993). https://doi.org/10.1029/93JB00356
64. Bar-Sinai, Y., Spatschek, R., Brener, E.A., Bouchbinder, E.: On the velocity-strengthening behavior of dry friction. J. Geophys. Res.: Solid Earth. **119**, 1738–1748 (2014). https://doi.org/10.1002/2013JB010586
65. Shroff, S.S., de Boer, M.P.: Full assessment of micromachine friction within the rate-state framework: experiments. Tribol. Lett. (2016). https://doi.org/10.1007/s11249-016-0718-3
66. Shroff, S.S., de Boer, M.P.: Full assessment of micromachine friction within the rate-state framework: theory and validation. Tribol. Lett. **63**, 39 (2016). https://doi.org/10.1007/s11249-016-0724-5
67. Kato, N.: A possible model for large preseismic slip on a deeper extension of a seismic rupture plane. Earth Planet. Sci. Lett. **216**, 17–25 (2003). https://doi.org/10.1016/S0012-821X(03)00483-7
68. Bouchbinder, E., Brener, E.A., Barel, I., Urbakh, M.: Slow cracklike dynamics at the onset of frictional sliding. Phys. Rev. Lett. **107**, 235501 (2011). https://doi.org/10.1103/PhysRevLett.107.235501
69. Hasz, K., Ye, Z., Martini, A., Carpick, R.W.: Experiments and simulations of the humidity dependence of friction between nanoasperities and graphite: the role of interfacial contact quality. Phys. Rev. Mater. **2**, 126001 (2018). https://doi.org/10.1103/PhysRevMaterials.2.126001
70. Ouyang, W., Ramakrishna, S.N., Rossi, A., Urbakh, M., Spencer, N.D., Arcifa, A.: Load and velocity dependence of friction mediated by dynamics of interfacial contacts. Phys. Rev. Lett. (2019). https://doi.org/10.1103/PhysRevLett.123.116102
71. Derjaguin, B.V., Muller, V.M., Toporov, Yu.P.: Effect of contact deformations on the adhesion of particles. J. Colloid Interface Sci. **53**, 314–326 (1975). https://doi.org/10.1016/0021-9797(75)90018-1
72. Chen, J., Ratera, I., Park, J.Y., Salmeron, M.: Velocity dependence of friction and hydrogen bonding effects. Phys. Rev. Lett. **96**, 236102 (2006). https://doi.org/10.1103/PhysRevLett.96.236102
73. Filippov, A.E., Klafter, J., Urbakh, M.: Friction through dynamical formation and rupture of molecular bonds. Phys. Rev. Lett. **92**, 135503 (2004). https://doi.org/10.1103/PhysRevLett.92.135503
74. Barel, I., Filippov, A.E., Urbakh, M.: Formation and rupture of capillary bridges in atomic scale friction. J. Chem. Phys. **137**, 164706 (2012). https://doi.org/10.1063/1.4762863
75. Ouyang, W., Urbakh, M.: Microscopic mechanisms of frictional aging.J. Mech. Phys. Solids **166**, 104944 (2022)
76. Ouyang, W., Cheng, Y., Ma, M., Urbakh, M.: Load-velocity-temperature relationship in frictional response of microscopic contacts. J. Mech. Phys. Solids **137**, 103880 (2020). https://doi.org/10.1016/j.jmps.2020.103880
77. Shao, Y., Jacobs, T.D.B., Jiang, Y., Turner, K.T., Carpick, R.W., Falk, M.L.: Multibond model of single-asperity tribochemical wear at the nanoscale. ACS Appl. Mater. Interfaces **9**, 35333–35340 (2017). https://doi.org/10.1021/acsami.7b08023
78. Zhuravlev, L.T.: The surface chemistry of amorphous silica. Zhuravlev model. Colloids Surf. A. **173**, 1–38 (2000). https://doi.org/10.1016/S0927-7757(00)00556-2

79. Dalstein, L., Potapova, E., Tyrode, E.: The elusive silica/water interface: isolated silanols under water as revealed by vibrational sum frequency spectroscopy. Phys. Chem. Chem. Phys. **19**, 10343–10349 (2017). https://doi.org/10.1039/C7CP01507K
80. Peng, L., Hsu, C.-C., Xiao, C., Bonn, D., Weber, B.: Controlling macroscopic friction through interfacial siloxane bonding. Phys. Rev. Lett. **131**, 226201 (2023). https://doi.org/10.1103/PhysRevLett.131.226201
81. Rimsza, J.M., Yeon, J., van Duin, A.C.T., Du, J.: Water interactions with nanoporous silica: comparison of ReaxFF and *ab Initio* based molecular dynamics simulations. J. Phys. Chem. C **120**, 24803–24816 (2016). https://doi.org/10.1021/acs.jpcc.6b07939
82. Ewing, C.S., Bhavsar, S., Veser, G., McCarthy, J.J., Johnson, J.K.: Accurate amorphous silica surface models from first-principles thermodynamics of surface dehydroxylation. Langmuir **30**, 5133–5141 (2014). https://doi.org/10.1021/la500422p
83. Warring, S.L., Beattie, D.A., McQuillan, A.J.: Surficial siloxane-to-silanol interconversion during room-temperature hydration/dehydration of amorphous silica films observed by ATR-IR and TIR-Raman Spectroscopy. Langmuir **32**, 1568–1576 (2016). https://doi.org/10.1021/acs.langmuir.5b04506
84. Lupton, E.M., Achenbach, F., Weis, J., Bräuchle, C., Frank, I.: Modified chemistry of siloxanes under tensile stress: interaction with environment. J. Phys. Chem. B **110**, 14557–14563 (2006). https://doi.org/10.1021/jp0607059
85. Kuwahara, T., Moras, G., Moseler, M.: Role of oxygen functional groups in the friction of water-lubricated low-index diamond surfaces. Phys. Rev. Mater. **2**, 073606 (2018). https://doi.org/10.1103/PhysRevMaterials.2.073606
86. Yeon, J., van Duin, A.C.T., Kim, S.H.: Effects of water on tribochemical wear of silicon oxide interface: Molecular Dynamics (MD) Study with Reactive Force Field (ReaxFF). Langmuir **32**, 1018–1026 (2016). https://doi.org/10.1021/acs.langmuir.5b04062
87. Comas-Vives, A.: Amorphous SiO_2 surface models: energetics of the dehydroxylation process, strain, *ab initio* atomistic thermodynamics and IR spectroscopic signatures. Phys. Chem. Chem. Phys. **18**, 7475–7482 (2016). https://doi.org/10.1039/C6CP00602G
88. Sang, Y., Dubé, M., Grant, M.: Thermal effects on atomic friction. Phys. Rev. Lett. **87**, 174301 (2001). https://doi.org/10.1103/PhysRevLett.87.174301
89. Dudko, O., Hummer, G., Szabo, A.: Intrinsic rates and activation free energies from single-molecule pulling experiments. Phys. Rev. Lett. **96**, 108101 (2006). https://doi.org/10.1103/PhysRevLett.96.108101
90. Schwaderer, P., Funk, E., Achenbach, F., Weis, J., Bräuchle, C., Michaelis, J.: Single-molecule measurement of the strength of a siloxane bond. Langmuir **24**, 1343–1349 (2008). https://doi.org/10.1021/la702352x
91. Vanossi, A., Bechinger, C., Urbakh, M.: Structural lubricity in soft and hard matter systems. Nat. Commun. **11**, 4657 (2020). https://doi.org/10.1038/s41467-020-18429-1
92. Zhai, W., Zhou, K.: Nanomaterials in superlubricity. Adv. Func. Mater. **29**, 1806395 (2019). https://doi.org/10.1002/adfm.201806395
93. Tian, K., Goldsby, D.L., Carpick, R.W.: Rate and state friction relation for nanoscale contacts: thermally activated Prandtl–Tomlinson model with chemical aging. Phys. Rev. Lett. **120**, 186101 (2018). https://doi.org/10.1103/PhysRevLett.120.186101
94. Craciun, A.D., Gallani, J.L., Rastei, M.V.: Stochastic stick–slip nanoscale friction on oxide surfaces. Nanotechnology **27**, 055402 (2016). https://doi.org/10.1088/0957-4484/27/5/055402
95. Riedo, E., Gnecco, E., Bennewitz, R., Meyer, E., Brune, H.: Interaction potential and hopping dynamics governing sliding friction. Phys. Rev. Lett. **91**, 084502 (2003). https://doi.org/10.1103/PhysRevLett.91.084502
96. Chen, L., Xiao, C., Yu, B., Kim, S.H., Qian, L.: What governs friction of silicon oxide in humid environment: contact area between solids, water meniscus around the contact, or water layer structure? Langmuir **33**, 9673–9679 (2017). https://doi.org/10.1021/acs.langmuir.7b02491
97. Zhu, T., Li, J., Lin, X., Yip, S.: Stress-dependent molecular pathways of silica–water reaction. J. Mech. Phys. Solids **53**, 1597–1623 (2005). https://doi.org/10.1016/j.jmps.2005.02.002
98. Tian, K.: Rate and state friction laws for interfacial chemical bond-induced friction at the nanoscale. Dissertations available from ProQuest. 1–124 (2017)
99. Li, Z., Szlufarska, I.: Physical origin of the mechanochemical coupling at interfaces. Phys. Rev. Lett. **126**, 076001 (2021). https://doi.org/10.1103/PhysRevLett.126.076001
100. Lupton, E.M., Nonnenberg, C., Frank, I., Achenbach, F., Weis, J., Bräuchle, C.: Stretching siloxanes: an *ab initio* molecular dynamics study. Chem. Phys. Lett. **414**, 132–137 (2005). https://doi.org/10.1016/j.cplett.2005.07.118
101. Chen, L., He, X., Liu, H., Qian, L., Kim, S.H.: Water adsorption on hydrophilic and hydrophobic surfaces of silicon. J. Phys. Chem. C **122**, 11385–11391 (2018). https://doi.org/10.1021/acs.jpcc.8b01821
102. Szoszkiewicz, R., Riedo, E.: Nucleation time of nanoscale water bridges. Phys. Rev. Lett. **95**, 135502 (2005). https://doi.org/10.1103/PhysRevLett.95.135502
103. Riedo, E., Lévy, F., Brune, H.: Kinetics of capillary condensation in nanoscopic sliding friction. Phys. Rev. Lett. **88**, 185505 (2002). https://doi.org/10.1103/PhysRevLett.88.185505
104. Cassin, F., Hahury, R., Lançon, T., Franklin, S., Weber, B.: The nucleation, growth, and adhesion of water bridges in sliding nano-contacts. J. Chem. Phys. **158**, 224703 (2023). https://doi.org/10.1063/5.0150276
105. Noel, O., Mazeran, P.-E., Nasrallah, H.: Sliding velocity dependence of adhesion in a nanometer-sized contact. Phys. Rev. Lett. **108**, 015503 (2012). https://doi.org/10.1103/PhysRevLett.108.015503